Placing High-Redshift Quasars in Perspective: a Catalog of Spectroscopic Properties from the Gemini Near Infrared Spectrograph - Distant Quasar Survey

Brandon M. Matthews,[1] Ohad Shemmer,[1] Cooper Dix,[1] Michael S. Brotherton,[2] Adam D. Myers,[2] I. Andruchow,[3,4] W. N. Brandt,[5,6,7] Gabriel A. Ferrero,[3,4] S. C. Gallagher,[8] Richard Green,[9] Paulina Lira,[10] Richard M. Plotkin,[11] Gordon T. Richards,[12] Jessie C. Runnoe,[13] Donald P. Schneider,[5,6] Yue Shen,[14,15,*] Michael A. Strauss,[16] and Beverley J. Wills[17]

[1]Department of Physics, University of North Texas, Denton, TX 76203, USA
[2]Department of Physics and Astronomy, University of Wyoming, Laramie, WY 82071, USA
[3]Facultad de Ciencias Astronómicas y Geofísicas, Universidad Nacional de La Plata, Paseo del Bosque, B1900FWA La Plata, Argentina
[4]Instituto de Astrofísica de La Plata, CONICET–UNLP, CCT La Plata, Paseo del Bosque, B1900FWA La Plata, Argentina
[5]Department of Astronomy and Astrophysics, The Pennsylvania State University, University Park, PA 16802, USA
[6]Institute for Gravitation and the Cosmos, The Pennsylvania State University, University Park, PA 16802, USA
[7]Department of Physics, 104 Davey Lab, The Pennsylvania State University, University Park, PA 16802, USA
[8]Department of Physics & Astronomy, University of Western Ontario, 1151 Richmond St, London, ON N6C 1T7, Canada
[9]Steward Observatory, University of Arizona, 933 N Cherry Ave, Tucson, AZ 85721, USA
[10]Departamento de Astronomía, Universidad de Chile, Casilla 36D, Santiago, Chile
[11]Department of Physics, University of Nevada, Reno, NV 89557, USA
[12]Department of Physics, Drexel University, 32 S. 32nd Street, Philadelphia, PA 19104, USA
[13]Department of Physics & Astronomy, Vanderbilt University, 6301 Stevenson Center Ln, Nashville, TN 37235, USA
[14]Department of Astronomy, University of Illinois at Urbana-Champaign, Urbana, IL 61801, USA
[15]National Center for Supercomputing Applications, University of Illinois at Urbana-Champaign, Urbana, IL 61801, USA
[16]Department of Astrophysical Sciences, Princeton University, Princeton, NJ 08544, USA
[17]University of Texas Astronomy Department, University of Texas at Austin, C1400, 1 University Station, Austin, TX 78712, USA

ABSTRACT

We present spectroscopic measurements for 226 sources from the Gemini Near Infrared Spectrograph - Distant Quasar Survey (GNIRS-DQS). Being the largest uniform, homogeneous survey of its kind, it represents a flux-limited sample ($m_i \lesssim 19.0$ mag, $H \lesssim 16.5$ mag) of Sloan Digital Sky Survey (SDSS) quasars at $1.5 \lesssim z \lesssim 3.5$ with a monochromatic luminosity (λL_λ) at 5100 Å in the range of $10^{44} - 10^{46}$ erg s^{-1}. A combination of the GNIRS and SDSS spectra covers principal quasar diagnostic features, chiefly the C IV $\lambda1549$, Mg II $\lambda\lambda2798, 2803$, Hβ $\lambda4861$, and [O III] $\lambda\lambda4959, 5007$ emission lines, in each source. The spectral inventory will be utilized primarily to develop prescriptions for obtaining more accurate and precise redshifts, black hole masses, and accretion rates for all quasars. Additionally, the measurements will facilitate an understanding of the dependence of rest-frame ultraviolet-optical spectral properties of quasars on redshift, luminosity, and Eddington ratio, and test whether the physical properties of the quasar central engine evolve over cosmic time.

Keywords: quasars: general — line: profiles — catalogs — surveys

1. INTRODUCTION

A persistent problem in extragalactic astrophysics is understanding how supermassive black holes (SMBHs)

brandonmatthews@my.unt.edu

* Alfred P. Sloan Research Fellow

and their host galaxies co-evolve over cosmic time (e.g., Di Matteo et al. 2008; Merloni et al. 2010; Bromm, & Yoshida 2011; Heckman, & Best 2014). This problem touches upon several aspects of galaxy evolution, including the SMBH mass ($M_{\rm BH}$), which correlates with properties of the host galaxy, such as the bulge mass and stellar velocity dispersion (e.g., Ferrarese, & Merritt 2000; Gebhardt et al. 2000; Woo et al. 2010; Kormendy,

& Ho 2013; McConnell, & Ma 2013; Reines, & Volonteri 2015), the accretion rate, which probes the accretion flow and efficiency of the accretion process, (e.g., Croton et al. 2006; Hopkins & Quataert 2010; Blaes 2014), and the kinematics of material outflowing from the vicinity of the SMBH, which may affect star formation in the host galaxy (e.g., Hopkins, & Elvis 2010; Maiolino et al. 2012; Carniani et al. 2018). For nearby ($z \lesssim 1$) active galactic nuclei (AGNs) or quasars, most of the parameters required for exploring these topics can be most reliably estimated using optical diagnostics, namely the broad Hβ $\lambda 4861$ and narrow [O III] $\lambda\lambda 4959$, 5007 emission lines. However, at $z \gtrsim 1$, which includes the epoch of peak quasar activity (from $z = 1-3$), these diagnostic emission lines are redshifted beyond $\lambda_{\mathrm{obs}} \sim 1\mu$m, firmly into the near-infrared (NIR) regime. Since the vast majority of large spectroscopic quasar surveys have been limited to $\lambda_{\mathrm{obs}} \lesssim 1\mu$m, investigations of large samples of quasars at $z \gtrsim 1$ are usually forced to use spectroscopic proxies for Hβ and [O III]. Using indirect proxies can lead not only to inaccurate redshifts (e.g., Gaskell 1982; Hewett, & Wild 2010; Denney et al. 2016b; Shen et al. 2016; Dix et al. 2020), but also to systematically biased and imprecise estimates of fundamental parameters such as M_{BH} and accretion rate (e.g., Trakhtenbrot, & Netzer 2012; Shen, & Liu 2012; Denney et al. 2016a).

NIR spectra have been obtained for a few hundred quasars at $z \gtrsim 1$, but these spectra constitute a heterogeneous collection of relatively small samples ($\approx 10 - 100$ sources) that span wide ranges of source-selection criteria, instrument properties, spectral band and resolution, and signal-to-noise ratio (S/N) (e.g., McIntosh et al. 1999; Shemmer et al. 2004; Sulentic et al. 2004; Netzer et al. 2007; Trakhtenbrot et al. 2011; Shen, & Liu 2012; Zuo et al. 2015; López et al. 2016; Mejía-Restrepo et al. 2016; Shen 2016; Coatman et al. 2017). Thus, the current NIR spectroscopic inventory for high-redshift quasars is biased in a multitude of selection criteria, and none of these mini-surveys are capable of providing a coherent picture of SMBH growth across cosmic time.

To mitigate the various systematic biases present in the current NIR spectroscopic inventory, we have obtained NIR spectra of 272 quasars at high redshift using the Gemini Near-Infrared Spectrograph (GNIRS, Elias et al. 2006), at the Gemini-North Observatory, with a Gemini Large and Long Program[1]. By utilizing spectroscopy in the ~ 0.8–2.5 μm band of a uniform, flux-limited sample of optically selected quasars

---

[1] http://www.gemini.edu/node/12726

at $1.5 \lesssim z \lesssim 3.5$, our Distant Quasar Survey (GNIRS-DQS) was designed to produce spectra that, at a minimum, encompass the essential Hβ and [O III] region in each source while having sufficient S/N in the NIR band to obtain meaningful measurements of this region. This survey assembles the largest uniform sample of $z \gtrsim 1$ quasars with rest-frame optical spectroscopic coverage. The spectral inventory presented in this catalog will allow development of single-epoch prescriptions, as opposed to C IV reverberation mapping, for rest-frame ultraviolet (UV) analogs of key properties such as M_{BH} and accretion rate, along with revised redshifts based primarily on emission lines in the rest-frame optical band.

This paper describes the GNIRS observations and structure of the catalog; subsequent investigations will present the scientific analyses enabled by this catalog. Section 2 describes the target selection, and Section 3 describes the GNIRS observations, and the spectroscopic data processing. Section 4 presents the catalog of basic spectral properties, along with a smaller catalog of additional features that can be measured reliably in some of the spectra. Section 5 summarizes the main properties of our catalog as well as comments on its future applications. Throughout this paper we adopt a flat ΛCDM cosmology with $\Omega_\Lambda = 1 - \Omega_0 = 0.7$ and $H_0 = 70 \ \mathrm{kms}^{-1}\mathrm{Mpc}^{-1}$ (Spergel et al. 2007).

2. TARGET SELECTION

The GNIRS-DQS targets were selected from the spectroscopic quasar catalog of the Sloan Digital Sky Survey (SDSS; York et al. 2000), primarily from SDSS Data Release 12 (Pâris et al. 2017) and supplemented by SDSS Data Release 14 (DR14; Pâris et al. 2018). Sources were selected to lie in three narrow redshift intervals, $1.55 \lesssim z \lesssim 1.65$, $2.10 \lesssim z \lesssim 2.40$, and $3.20 \lesssim z \lesssim 3.50$, in order to cover the Hβ+[O III] emission complex, and in order of decreasing NIR brightness, down to $m_i \sim 19.0$, a limit at which the SDSS is close to complete in each of those redshift intervals (Richards et al. 2002). Figure 1 displays the luminosity-redshift distribution of GNIRS-DQS sources with respect to sources from the SDSS DR14 catalog. For the redshift distributions in the selected intervals, shown in Figure 2 along with their respective magnitude distributions, the Hβ+[O III] emission complex reaches the highest S/N in the centers of the J, H, and K bands, respectively. The selected redshift intervals also ensure coverage of sufficient continuum emission and Fe II line emission flanking the Hβ+[O III] complex, enabling accurate fitting of these features. We visually inspected the SDSS spectrum of each candidate and removed sources hav-

ing spurious redshifts, instrumental artifacts, and other anomalies. The combined SDSS-GNIRS spectroscopic coverage of each source includes, at a minimum, the C IV $\lambda1549$, Mg II $\lambda\lambda2796$, 2803, Hβ, and [O III] emission lines; the Hα $\lambda6563$ emission line is present in all sources at $1.55 \lesssim z \lesssim 2.50$, representing $\sim 87\%$ of our sample. We note that the $2.10 \lesssim z \lesssim 2.40$ redshift bin comprises $\sim 67\%$ of our entire sample, given that this redshift bin is three times wider than that of the lower redshift bin, and sources in this bin are brighter than the sources in the higher redshift bin.
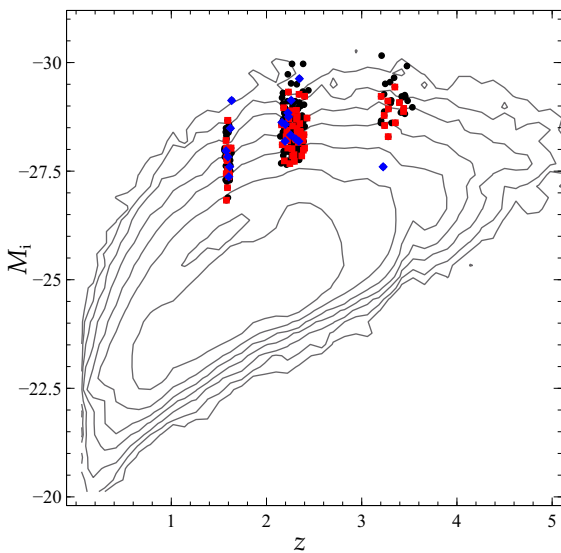
radio quiet quasars[2] (comprising $\sim 30\%$[3] and $\sim 12\%$ of the sample, respectively; Pâris et al. 2018). Figure 3 shows the radio loudness distribution of the GNIRS-DQS sources. The GNIRS-DQS sample is broadly representative of the general quasar population of luminous, high-redshift quasars during the epoch of most intense quasar activity (e.g., Hewett et al. 1993; Hasinger et al. 2005; Richards et al. 2006).

Figure 1. Distribution of SDSS quasars from DR14 (contours) and the 272 objects in the GNIRS-DQS sample (symbols) in the luminosity-redshift plane, where M_i is the absolute i-band luminosity (BAL quasars are represented by red squares, and non-radio quiet quasars are represented by blue diamonds). Most, but not all, quasars in DR14 are represented via contour lines, for clarity. Redshift ranges were chosen to ensure the prominent emission lines of Hβ and [O III] would be centered in the J, H, or K band. The final sample is representative of the quasar population within our selection criteria.

Figure 2. Redshift distribution in each redshift interval from SDSS (top), and corresponding magnitude distribution of the 272 objects in our sample (bottom). The three redshift bins correspond to the Hβ and [O III] lines appearing at the center of the J, H, or K photometric bands.

In summary, the GNIRS-DQS sources constitute an optically-selected, NIR flux limited sample of quasars, spanning wide ranges in rest-frame UV spectral properties, including broad absorption line (BAL) and non-

[2] We consider radio-quiet quasars to have $R < 10$, where R is the radio loudness, defined as $R = f_\nu(5 \text{ GHz}) / f_\nu (4400 \text{ Å})$, where $f_\nu(5 \text{ GHz})$ and $f_\nu(4400 \text{ Å})$ are the flux densities at rest-frame frequencies of 5 GHz and 4400 Å, respectively (Kellermann et al. 1989). Non-radio quiet quasars include radio-intermediate ($10 < R < 100$) and radio-loud ($R > 100$) sources, respectively.

[3] Quasars flagged as BAL quasars in Pâris et al. (2018) (see, Table 1).
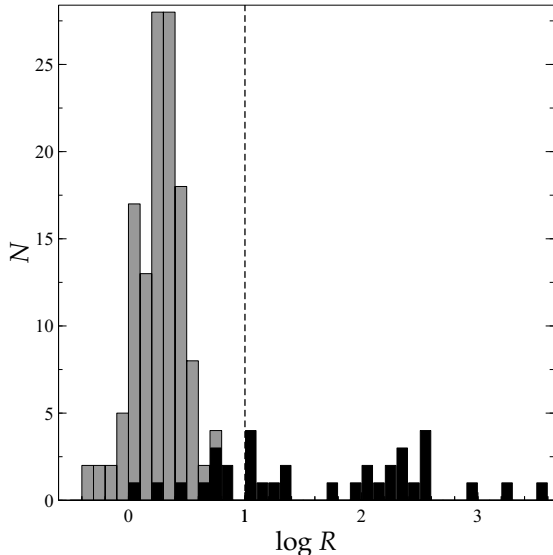
Figure 3. Radio loudness distribution of the GNIRS-DQS sources; the shaded (grey) columns represent upper limits on R for radio undetected sources based on the Pâris et al. (2018) catalog, and the dashed line at $\log R = 1$ incidates the threshold for radio quiet quasars. This distribution is generally similar to that of the SDSS quasar population (e.g., Richards et al. 2006).

3. OBSERVATIONS, AND DATA REDUCTION

The observations were designed to yield data of roughly comparable quality, in terms of both S/N and spectral resolution, to the respective SDSS spectra at $\lambda_{\rm obs} \sim 5000$ Å. The GNIRS spectra were thus required to have a ratio of ~ 40 between the mean flux density and the standard deviation of that flux density in a rest-frame wavelength interval spanning 100 Å around $\lambda_{\rm rest} = 5100$ Å, and a spectral resolution of $R \sim 1100$ across the entire GNIRS band. These requirements enable accurate measurements of redshift based on [O III] line peaks, with the high S/N contributing to reducing the uncertainties below the spectral resolution limit, ~ 300 km s^{-1} (Shen et al. 2016). As explained below in Section 4, we determine that, on average, our spectra produce uncertainties on the measured line peak of [O III] $\lambda5007$ of order ~ 50 km s^{-1}, stemming from pixel-to-wavelength calibration and our fitting procedures.

All spectra were obtained in queue observing mode with GNIRS configured to use the Short Blue camera ($0.15''$pix^{-1}), the 32 lines mm^{-1} grating in cross-dispersed mode, and the $0.45''$-wide slit. This configuration covers the observed-frame $\sim$0.8–2.5 μm band in each source, simultaneously, in six spectral orders with overlapping spectral coverage. Our observing strategy utilized an ABBA method of slit nodding to enable sky

subtraction. Exposure times ranged from $\sim 10 - 40$ minutes for each object, with an additional 15 minutes of overhead per source. Each observation included calibration exposures, and either one or two ABBA sequences depending on source brightness. We also observed a telluric standard star either immediately before or after the observation in a spectral range of B8 V to A4 V, with $8200\,{\rm K} \lesssim T_{\rm eff} \lesssim 13000\,{\rm K}$, and typically within $\approx 10° - 15°$ from each quasar.

The observation log of the original 272 sources appears in Table 1. Column (1) is the SDSS designation of the quasar. Column (2) provides the most reliable reported redshift estimate from SDSS (Pâris et al. 2018, Table A1, column 9 "Z"). Columns (3), (4), and (5) list the respective J, H, and K magnitudes of each quasar from the Two Micron All Sky Survey (2MASS; Skrutskie et al. 2006). Columns (6) and (7) give the observation date and semester, respectively. Column (8) is the net science exposure time, Column (9) provides comments, if any, concerning the observation, Column (10) provides a flag for whether or not the quasar is a BAL quasar (as defined in Pâris et al. 2018), and Column (11) provides a flag for whether or not the quasar is considered non-radio quiet (see, footnote 2).

We classify an acceptable observing night for this survey based on our programs' approved observing conditions including no greater than 50% cloud cover and 85% image quality[4], however some objects were observed under worse conditions, and are noted as such in Table 1. Additionally, 12 sources were observed over two observing sessions. These additional observations are recorded separately and immediately follow the initial observation in Table 1 (which brings the total number of lines in that Table to 284). For these objects, all available observations were utilized in the reduction process.

Our data processing procedure generally follows the XDGNIRS pipeline developed by the Gemini Observatory (Mason et al. 2015[5]: see also Shen et al. 2019b) with the Gemini package in PyRAF[6]. Following standard image cleaning for artifacts and other observational anomalies, we pair-subtract the images to remove the bulk of the background noise by directly combining the sky-subtracted object exposures. Quartz lamps and IR lamps were used to create flat fields to correct pixel-by-pixel variation across the detector. The flat-fielded images were corrected for optical distortions. Several ob-

---

[4]   https://www.gemini.edu/observing/telescopes-and-sites/sites#Constraints

[5]   http://www.gemini.edu/sciops/instruments/gnirs/data-format-and-reduction/reducing-xd-spectra

[6] https://www.gemini.edu/node/11823

jects required replacement flat fields due to pixel shifting of dead pixels in the detector into the GNIRS spectra directly (marked accordingly with a corresponding comment in Table 1), which produced a notable increase in the uncertainty of spectroscopic measurements for these objects, particularly in the bluer bands. On average, the increased flux uncertainty from these spectra is on the order of ∼3%. At this stage, of the 272 sources observed, 46 observations did not yield a meaningful spectrum due to bad weather, instrument artifacts, or other technical difficulties (Note 4 in Column 9 of Table 1), leaving the final sample at 226 sources.

Wavelength calibration was performed using two argon lamp exposures in order to assign wavelength values to the observed pixels. The uncertainties associated with this wavelength calibration are not larger than 0.5 Å RMS, corresponding to $\lesssim 10$ km s^{-1} at ∼ 15000 Å.

Spectra of the telluric standards were processed in a similar fashion, followed by a careful removal of the stars' intrinsic hydrogen absorption lines. This process was performed by fitting Lorentzian profiles to the hydrogen absorption lines, and interpolating across these features to connect the continuum on each side of the line. Following the line cancellation, the quasar spectra were divided by the corrected stellar spectra. The corrected spectra were multiplied by an artificial blackbody curve with a temperature corresponding to the telluric standard star, which yielded a cleaned, observed-frame quasar spectrum. Each quasar spectrum was flux calibrated by comparing local flux densities to the J, H, and K 2MASS magnitudes from Table 1 and using the magnitude-to-flux conversion factors from Table A.2 of Bessell et al. (1998). For the final spectra, we masked any noise present from cosmic rays, regions of high levels of atmospheric absorption, and band gap interference.

We chose this method as opposed to flux calibrating via the telluric standards to avoid any differences in atmospheric conditions between observations of the object and the telluric standard. This preference was also motivated by our use of a relatively narrow slit in order to prioritize spectral resolution at the cost of potentially larger slit losses in the observations. Although the 2MASS and Gemini observations are separated by several years in the quasars' rest frames, the cross-calibrations are subject to minimal uncertainties since ∼ 88% of our sources are luminous radio-quiet quasars at high redshift. Such sources typically show UV-optical flux variations on the order of $\lesssim 10\%$ over such timescales (e.g., Vanden Berk et al. 2004; Kaspi et al. 2007; MacLeod et al. 2012). In fact, the effects stemming from the differences in airmass between the quasars and their respective telluric

standard stars, as well as the slit losses, are typically larger than the expected intrinsic quasar variability.

In order to further test the reliability of our flux calibration, we compared the flux densities in overlapping continuum regions, $\lambda_{\rm obs} \sim 8000 - 10000$ Å, between our GNIRS spectra and those of the respective SDSS spectra; this test was feasible for ∼ 90% of our sources that have both high-quality GNIRS and SDSS spectral data where we can obtain meaningful comparisons that avoid reductions in quality that can occur in this region for both surveys. We found that the flux densities in the SDSS spectra are, on average, smaller than the GNIRS flux densities by ∼ 40% ($\mu = -0.155$), with a 1σ scatter of ∼ 60% ($\sigma = 0.2013$) (see, Fig. 4, where μ and σ are the logarithms of the mean and standard deviation, respectively). Therefore, the flux densities when directly comparing both spectral sets are consistent at the 1σ level, despite the presence of this systematic offset. This systematic offset should be taken into account when comparing fluxes between SDSS and GNIRS spectra, however, it does not affect the emission-line measurements presented in this survey. This scatter may include discrepancies such as those due to intrinsic quasar variability, fiber light loss in SDSS spectra, and differences in airmass between quasars and their respective standard star observations. Examples of prominent emission lines in final, flux-calibrated spectra appear in Figure 5.
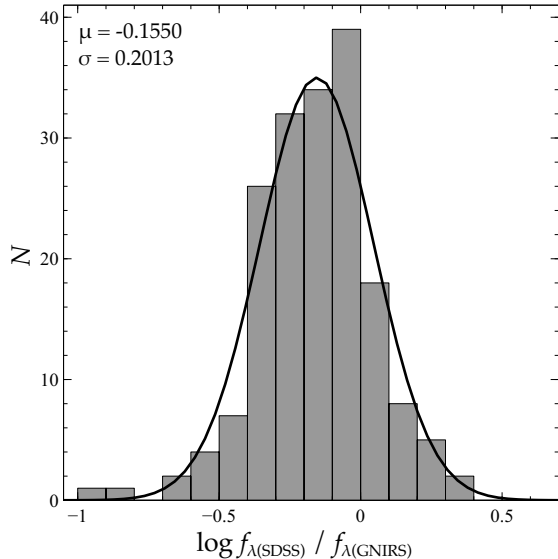
Figure 4. Flux-density ratio distribution between SDSS and GNIRS spectra from the overlapping continuum regions ($\lambda_{\rm obs} \sim 8000 - 10000$ Å) with a lognormal distribution fit. The log of the mean ratio (μ) and its standard deviation (σ) indicate that the flux densities of the GNIRS spectra are consistent at the 1σ level with those from their respective SDSS spectra.

4. SPECTRAL FITTING

The final GNIRS quasar spectra were fit by using multiple localized linear continua, explained in Section 4.1, constrained by no less than six narrow (~ 200 Å-wide, rest-frame) line-free regions, and performed Gaussian fits to the emission lines. The Fe II and Fe III emission complexes were modeled via empirical templates from Boroson, & Green (1992) and Vestergaard & Wilkes (2001) for the rest-frame optical and UV band, respectively. These templates were scaled and broadened by convolving a Gaussian with a full width at half maximum (FWHM) value that was free to vary between 1300 and 10000 km s^{-1}. Given that the Fe II, Fe III, and Hβ lines likely originate from different physical regions (e.g., Barth et al. 2013), we kept the FWHM of the iron templates as a free parameter. The FWHM values selected to broaden each template were determined using a least squares analysis on each fitted region.

For the [O III] lines, the widths of each line were restricted to be identical to each other, and their flux ratios were kept constant at $I_{5007}/I_{4959} = 3$ (e.g., Storey & Zeippen 2000, and references therein); additionally, the rest-frame wavelength difference between the $\lambda5007$ and $\lambda4959$ lines was kept constant, which proved adequate for the fits of each object.

We fit two Gaussians to each broad emission line profile to accommodate possible asymmetry present in the profile due to, e.g., absorption, or outflows. We note that the two Gaussians fit per broad emission-line are adopted for fitting purposes only, and they do not represent physically distinct regions. Fitting the line profiles with more complex models was not warranted given the quality of our GNIRS spectra. The constraints on the Gaussian profiles for each emission line were that the peak wavelengths can differ from their known rest-frame values by up to $\pm$ 1500 km s^{-1}, on initial assessment (see, e.g., Richards et al. 2011, Figure 5) with a max flux value ranging from zero to a value calculated to be twice the maximum value of the emission line. Visual inspection yielded some exceptions beyond an offset of $\pm$ 1500 km s^{-1}, whereupon manual fitting was performed to compensate for the larger velocity offset.

4.1. *Continuum Fitting*

By using localized linear continuum fitting, we were able to achieve more accurate measurements by avoiding uncertainties stemming from a single power-law fit. There has been debate about an accurate model for quasar continua: a single power-law, a broken power-law (e.g., Vanden Berk et al. 2001), or whether the power-law description is appropriate at all in the rest-frame optical band; for example, in highly reddened quasar spectra a single power-law fitting will likely fail (see, e.g., Shen et al. 2019a). Alternatively, quasar continua may be better described by accretion disk modeling (e.g., Mejía-Restrepo et al. 2016). This survey was primarily concerned with measuring emission-line properties as opposed to continua, and, through using a variety of fitting methods including our own investigations into the efficacy of power-law and broken power-law fits, we conclude that localized linear continua give, at worst, the same level of uncertainty as power-law fitting, and, at best, avoid large uncertainties inherent in modeling blended continuum features. Therefore, measurements of all the emission lines implemented localized linear continua where the windows for fitting were determined by the availability of the nearest continuum band segments as defined in Vanden Berk et al. (2001).

4.2. *Mg II*

The Mg II doublet is detected in the bluer regions of our spectra, where the S/N is lower by roughly an order of magnitude than the redder regions where the Hβ line is detected. Since our survey was designed such that the S/N near the Hβ region would be roughly comparable to the S/N across the respective SDSS spectrum of each source (see, Section 2), the S/N around the Mg II region
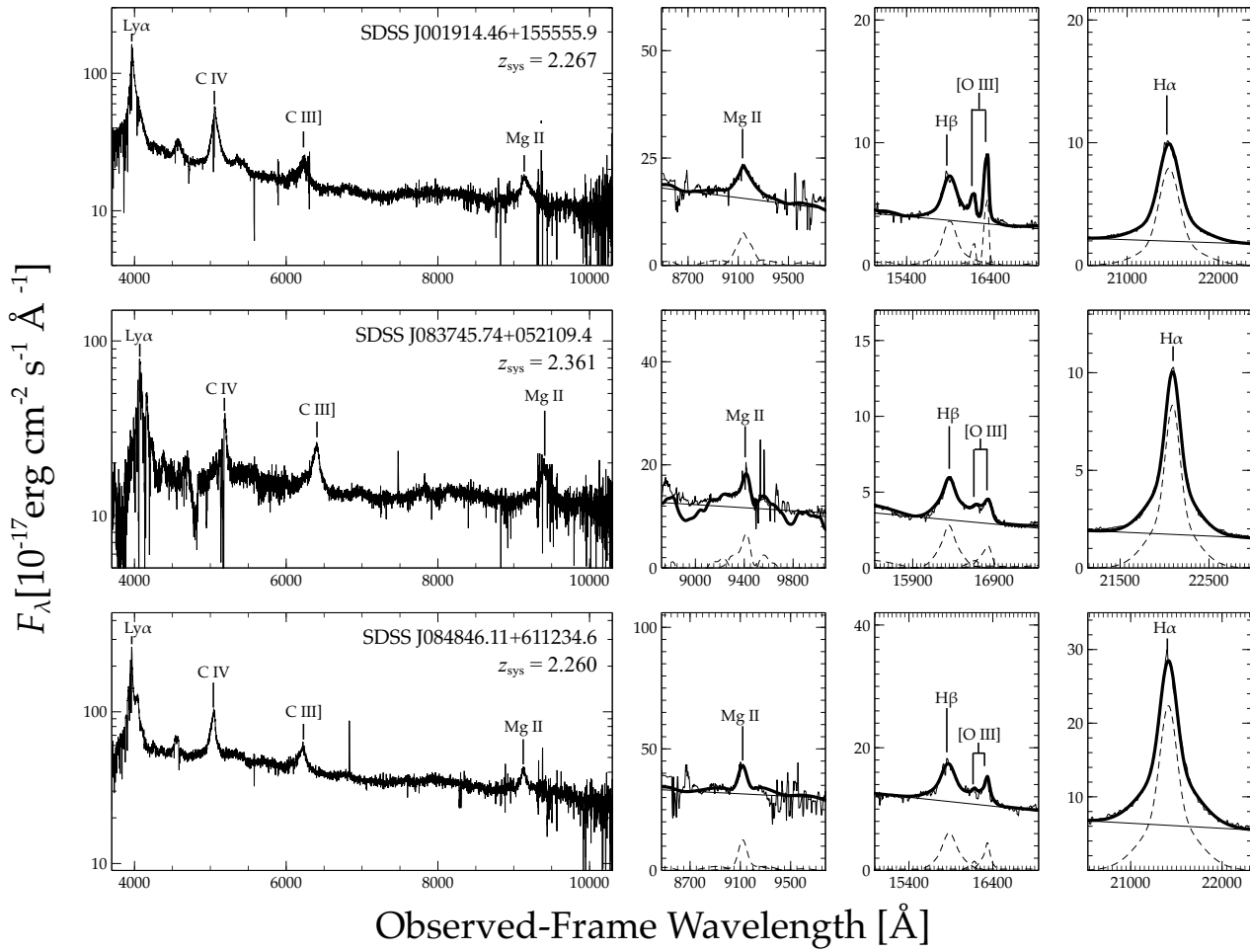
Figure 5. SDSS and GNIRS spectra and their best-fit models for three representative quasars in our sample (fitting of the SDSS spectra is deferred to a future publication). From left to right, panels show the corresponding SDSS spectra, followed by the GNIRS Mg II, Hβ, and Hα spectral regions, respectively. In the three rightmost panels, the spectrum is presented by a thin solid line, and best-fit models for the localized linear continua, Gaussian profiles, and iron emission blends are marked by dashed lines. Summed best-fit model spectra are overplotted with thick solid lines. Details of the spectral fitting procedure are given in Section 4. All of the GNIRS spectra and their best-fit models are available electronically at http://physics.uwyo.edu/agn/GNIRS-DQS/spectra.html. We note that SDSS J083745.74+052109.4 is flagged as a BAL quasar (see, Table 1, Pâris et al. 2017), and will be discussed in a future publication.

in our GNIRS spectra is roughly an order of magnitude lower than the corresponding values in the SDSS spectra. As a result, we were only able to obtain reliable Mg II and Fe II+Fe III fits for ~31% of our sources (and we do not present measurements for Fe II+Fe III due to their considerable uncertainties). In this work, we only present Mg II line measurements based on the GNIRS spectra of our sources; in a future publication, we will complement these data with Mg II line measurements based on the sample's SDSS spectra (for ~87% of our sample at $z \lesssim 2.4$). On average, the uncertainties on the measured Mg II properties are roughly an order of magnitude larger than those of Hβ. During

the fitting process, we made a preliminary evaluation of the noise around the Hβ and Mg II lines. If the noise around Mg II was within a defined threshold ($S/N \sim 10$) when compared to that of the Hβ region ($S/N \sim 40$, see Section 3), the Mg II line was fit automatically. Otherwise, each spectrum was visually inspected to determine if it was possible to perform reliable measurements of the Mg II line. Due to the lower S/N in this region, the Fe II+Fe III complex was fit with narrow (~ 20 Å) continuum bands and often required further interactive adjustments in order to avoid noise spikes to ensure accurate fitting to the Mg II feature.

4.3. Hβ

The Hβ region, for most of our objects, provided reliable measurements given the survey was designed with this region in mind. However, in $\lesssim 2\%$ of our objects, the Hβ emission line was adjacent to the edge of the observing band, resulting in larger uncertainties when fitting the Fe II emission complex. This misalignment of Hβ stems from selecting our sample using UV-based redshifts, based primarily on the peak wavelength of the C IV emission line, which suffer from systematic biases due to outflows that can be as large as ≈ 5000 km s^{-1} (Dix et al. 2020, Matthews et al., in prep., 2021). This misalignment also results in reduced coverage of the Fe II blends for these objects. Despite this complication, we were able to adequately fit two Gaussians to each of the Hβ emission lines.

By design, our survey targeted highly luminous quasars, biased toward having higher $L/L_{\rm Edd}$ values (see, Fig. 1, Netzer 2003), which typically also tend to have relatively strong Fe II emission. As a result, we relied on the broad iron bumps on either side of the Hβ line, rest-frame $\sim 4450 - 4750$ Å and $5100 - 5400$ Å (Vanden Berk et al. 2001), as our primary region for fitting the Fe II complex. While reasonable in most cases, these fits are likely affected by He II λ4686 emission-line contamination, however the He II emission line is unresolvable in this sample due to uncertainties from a variety of factors (see Section 4.5). On average, the corresponding Fe II EW values in those sources is ~ 20 Å. Additionally, $\sim 5\%$ of our objects differed from the well-known trends of "Eigenvector 1" (Boroson, & Green 1992), having a blend of strong [O III] and Fe II emission, resulting in their spectra exhibiting "shelves" on the red side of the Hβ profile. These features required a more careful fitting, and we did not see any evidence of [O III] outflows directly contributing to this emission complex. An example of a shelf-like fit is presented in Figure 6.
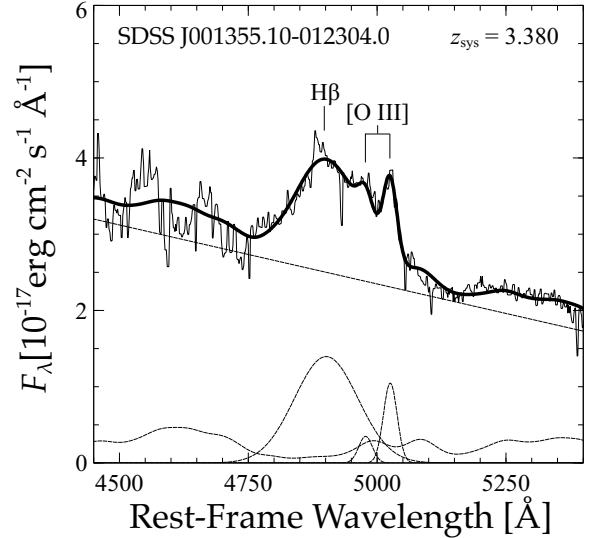
Figure 6. GNIRS spectrum of the Hβ region of SDSS J001315.10-012304.0, $z_{sys} = 3.380$. The "shelf" structure redward of the Hβ line appears to be a result of strong Fe II and mild [O III] emission. This differs from typical "Eigenvector 1" trends in Boroson, & Green (1992), where sources with strong Fe II blends tend to have weak [O III] lines. Line styles are as in Fig. 5. These shelves may be a signature of binary quasar candidates (see, e.g., Eracleous & Halpern 1994)

Figure 7 shows the distribution of [O III] EWs in the GNIRS-DQS sample. As explained in Section 4.6 below, for those objects that do not have detectable [O III] emission, we must use the Mg II line to determine systemic redshifts ($z_{\rm sys}$); for those objects that lack both [O III] and Mg II, we must utilize the Hβ line for that purpose, which is present in every GNIRS-DQS spectrum.
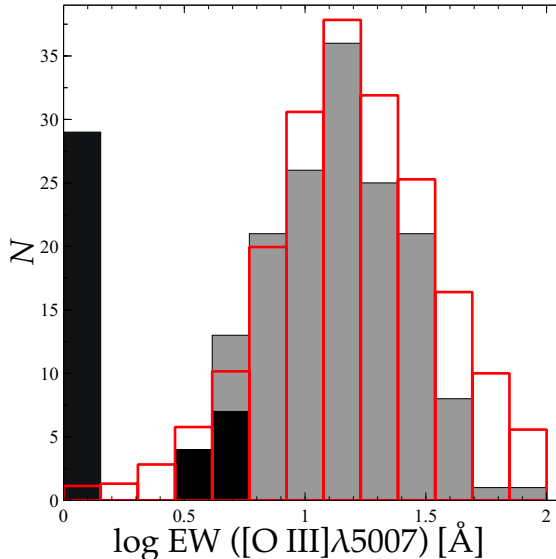
Figure 7. [O III] rest-frame EW distribution of the GNIRS-DQS sources (grey) overplotted with rest-frame [O III] EWs from Shen et al. (2011) (red outline; scaled down by a factor of 100). For $\sim 19\%$ of the GNIRS-DQS sources that lack detectable [O III] emission we are able to place strong upper limits on their EW values (black). When compared to [O III] measurements of low-redshift, low-luminosity sources from Shen et al. (2011), the [O III] emission tends to become weaker as luminosity increases, consistent with the trends observed in previous studies of high-redshift quasars (e.g., Netzer et al. 2004; Shen 2016).

4.4. $H\alpha$

Being the most prominent feature in all the spectra of our sources at $z < 2.5$ (constituting $\sim 87\%$ of the sample), Hα yielded the smallest uncertainties on all the emission-line parameters. We do not detect significant narrow [N II] emission-lines flanking the Hα line in any of our sources, which is expected given our selection of highly luminous quasars (e.g., Wills & Browne 1986; Shen et al. 2011).

4.5. *Uncertainties in Spectral Measurements*

The uncertainties inherent in the GNIRS spectra are contributed by a variety of factors. These include (but are not limited to) sub-par observing conditions, the use of replacement flat fields in several of the spectra (see Section 3), and differences in airmass and/or atmospheric conditions between the standard star and the respective quasar observations. Moreover, modeling the telluric standard star continuum with a blackbody function fails to account for potential NIR excess emission from a circumstellar disk around the star. These factors lead to uncertainties on the flux density and shapes of the emission-line profiles, including the locations of their peaks. The uncertainties on these parameters are

in the range $\approx$ 4-7%, $\approx$ 3-6%, $\approx$ 2-5%, and $\approx$ 2-4%, for each emission line, respectively. On average, these uncertainties result in general measurement errors across all parameters for an emission-line profile of up to $\sim 7\%$.

Emission-line fitting first relied on shifting the spectrum to the rest-frame using the best available SDSS redshift. However, due to inaccuracies with the SDSS redshift, the emission-lines in the GNIRS spectra often did not line up with the known rest-frame values. This offset led to uncertainties during fitting, and was ultimately mitigated by introducing a redshift iteration process. Emission-lines were fit for three different regimes separately, the Mg II, Hβ, and Hα regions, based off of the SDSS redshift. A systemic redshift, z_{sys}, was then determined by the best fit of the most reliable emission-line for measuring redshift, as discussed in Section 4.6 below, and the spectrum was shifted according to this value. This process was repeated until the difference in consecutive redshifts was less than $z_{n-1} - z_n < 0.001$ for each region. Additionally, this redshift iteration allows more accurate measurements on z_{sys}, the flux density at rest-frame 5100 Å ($F_{\lambda,5100}$), and more accurate fitting of the broadened iron templates.

After identifying the most accurate redshift, final fits are performed on emission-line features. Using preliminary Gaussian and localized linear continuum fits, residuals are generated, which yield upper and lower values for uncertainties present across the fitting region. With these residual bounds, Gaussian noise is introduced, and a series of 50 fits is performed in order to generate upper and lower bound estimates on the final Gaussian fits. To quantify the error on best-fit parameters, each iterated fit value is stored, which is used to generate a distribution of principle measurements. These distributions are then fit using a Gaussian function in order to determine the final errors at a 1σ confidence level. The iron templates of the Hβ and Mg II regions also experience iterations of FWHM for the line profile, which allows for accurate Fe II and Fe III broadening error estimates. These various fitting iterations allow conservative error estimates on basic emission-line parameters, i.e., FWHM, EW, and line peaks. Finally, the best fit spectral model for each source was verified by visual inspection.

4.6. *The Catalog*

Table 2 describes the format of the data presented in the catalog. It contains basic emission line properties, particularly the FWHM and rest-frame EW, of the Mg II, Hβ, [O III], and Hα emission lines. The catalog also provides observed-frame wavelengths of emission-line peaks, as well as the asymmetry and kurtosis of each

emission line, which were obtained from the Gaussian fits. A host of additional parameters are given, including the FWHM of the kernel Gaussian used for broadening the Fe II blends around the Hβ region and the EW of these blends in the $4434 - 4684$ Å region (following Boroson, & Green 1992), as well as the flux density and monochromatic luminosity (λL_λ) at 5100 Å. The catalog also provides $z_{\rm sys}$ values measured from observed-frame wavelengths of emission-line peaks. For determining $z_{\rm sys}$, we adopt the observed-frame wavelength of the peak of one of three emission lines with the highest degree of accuracy which is present in the GNIRS spectrum, where it is known that these three emission lines have uncertainties of $\simeq 50$ km s^{-1}, $\simeq 200$ km s^{-1}, and $\simeq 400$ km s^{-1} for [O III], Mg II, and Hβ, respectively (Shen et al. 2016).

In cases where the prominent emission lines (i.e., Mg II, Hβ, [O III], and Hα) have no significant detections, upper limits are placed on their EWs by assuming FWHM values for each line using the median value in the sample distributions, and taking the weakest feature detectable in the GNIRS spectra for each line. Additionally, we placed upper limits on the EW of the optical Fe II blends in cases where excess noise surrounding the Hβ+[O III] region would not enable us to fit the Fe II blends reliably; we found that a value of 2 Å for this parameter provides a conservative upper limit in all such cases.

Finally, additional, and typically weaker, emission line measurements follow the formatting presented in Table 3, and are reported in the supplemental features catalog for 106 sources from our sample where such features could be measured reliably. These emission lines were fit on a case-by-case basis after visually inspecting each GNIRS spectrum (and no upper limits are assigned in cases of non-detections). Where applicable, we performed fits on the following emission lines with two Gaussians per line, following the same methodology used for primary emission line measurements: Hδ $\lambda4101$, Hγ $\lambda4340$, and [Ne III] $\lambda3871$. The [O II] $\lambda3727$ doublet was fit in the same manner.

5. SUMMARY

We present a catalog of spectroscopic properties obtained from NIR observations of a uniform, flux-limited sample of 226 SDSS quasars at $1.5 \lesssim z \lesssim 3.5$, which is the largest, uniform inventory for such sources to date. The catalog includes basic spectral properties of Mg II, Hβ, [O III], Fe II, and Hα emission lines, as well as Hδ, Hγ, [O II], and [Ne III] emission lines for a subset of the sample. A spectral resolution of $R \sim 1,100$ was achieved for this data set, which is roughly comparable

to the value of the corresponding SDSS spectra. These measurements provide a database to comprehensively analyze and investigate rest-frame UV-optical spectral properties for high-redshift, high-luminosity quasars in a manner consistent with studies of low-redshift quasars.

In particular, the catalog will enable future work on robust calibrations of UV-based proxies to systemic redshifts and black-hole masses in distant quasars. Such prescriptions are becoming increasingly more important as millions of quasar optical spectra will be obtained in the near future by, e.g., the Dark Energy Spectroscopic Instrument (DESI; Levi et al. 2013; DESI Collaboration et al. 2016) and the 4-metre Multi-Object Spectroscopic Telescope (4MOST; de Jong et al. 2012), where reliable estimates of z_{sys} and $M_{\rm BH}$ will be crucial to extract the science value from these surveys. In forthcoming papers we will present, among other facets, redshift calibrations via indicative emission lines such as [O III] (Matthews et al., in prep.), SMBH estimates using the Hβ and Mg II profiles measured in this survey (Dix et al., in prep.), and correlations among UV-optical emission lines (e.g., Boroson, & Green 1992; Wills et al. 1999; Shen, & Liu 2012).

In the future, we should continue to push the redshift barrier for the Hβ and [O III] emission lines, as current investigations have been confined to $z \lesssim 3.5$, in order to gain an increased understanding of the co-evolution of SMBHs and their host galaxies, along with more reliable redshifts. However, at redshifts higher than $z \sim 3.5$, these observations cannot be obtained via ground-based telescopes. Future studies in this respect could include a two-pronged approach using small calibration surveys. The first survey, for example, can use higher resolution instruments such as Gemini's Spectrograph and Camera for Observations of Rapid Phenomena in the Infrared and Optical (SCORPIO; Robberto et al. 2018) which will better measure weak emission-line profiles and obtain more accurate measurements of the prominent emission lines. This information will reinforce the measurements of this survey and allow for more confident applications to much higher redshifts, even beyond $z > 6$. The second survey would be a select sample of a few dozen highly luminous $z > 3.5$ objects using space-based observations from the James Webb Space Telescope (JWST, Gardner et al. 2006) for optimal spectral quality, with the possibility for a contemporaneous SCORPIO survey to obtain measurements of lines such as C IV from the ground.

REFERENCES

Barth, A. J., Pancoast, A., Bennert, V. N., et al. 2013, ApJ, 769, 128

Bessell, M. S., Castelli, F., & Plez, B. 1998, A&A, 333, 231

Blaes, O. 2014, SSRv, 183, 21

Blandford, R. D., & McKee, C. F. 1982, ApJ, 255, 419

Boroson, T. A., & Green, R. F. 1992, ApJS, 80, 109

Bromm, V., & Yoshida, N. 2011, ARA&A, 49, 373

Carniani, S., Maiolino, R., Marconi, A., et al. 2018, AGN13: Beauty and the Beast. The 13th Italian Meeting on Active Galactic Nuclei, 68

Coatman, L., Hewett, P. C., Banerji, M., et al. 2017, MNRAS, 465, 2120

Croton, D. J., Springel, V., White, S. D. M., et al. 2006, MNRAS, 365, 11

Denney, K. D., Pogge, R. W., Assef, R. J., et al. 2013, ApJ, 775, 60

Denney, K. D., Horne, K., Shen, Y., et al. 2016, ApJS, 224, 14

Denney, K. D., Horne, K., Brandt, W. N., et al. 2016, ApJ, 833, 33

DESI Collaboration, Aghamousa, A., Aguilar, J., et al. 2016, arXiv e-prints, arXiv:1611.00036

Di Matteo, T., Colberg, J., Springel, V., et al. 2008, ApJ, 676, 33

Dix, C., Shemmer, O., Brotherton, M. S., et al. 2020, ApJ, 893, 14

Elias, J. H., Joyce, R. R., Liang, M., et al. 2006, Proc. SPIE, 6269, 62694C

Eracleous, M. & Halpern, J. P. 1994, ApJS, 90, 1

Ferrarese, L., & Merritt, D. 2000, ApJ, 539, L9

Gardner, J. P., Mather, J. C., Clampin, M., et al. 2006, SSRv, 123, 485

Gaskell, C. M. 1982, ApJ, 263, 79

Gebhardt, K., Bender, R., Bower, G., et al. 2000, ApJ, 539, L13

Hasinger, G., Miyaji, T., & Schmidt, M. 2005, A&A, 441, 417

Heckman, T. M., & Best, P. N. 2014, ARA&A, 52, 589

Hewett, P. C., Foltz, C. B., & Chaffee, F. H. 1993, ApJL, 406, L43

Hewett, P. C., & Wild, V. 2010, MNRAS, 405, 2302

Hopkins, P. F., & Elvis, M. 2010, MNRAS, 401, 7

Hopkins, P. F. & Quataert, E. 2010, MNRAS, 407, 1529

de Jong, R. S., Bellido-Tirado, O., Chiappini, C., et al. 2012, Proc. SPIE, 8446, 84460T

Kaspi, S., Brandt, W. N., Maoz, D., et al. 2007, ApJ, 659, 997

Kellermann, K. I., Sramek, R., Schmidt, M., et al. 1989, AJ, 98, 1195

Kormendy, J., & Ho, L. C. 2013, ARA&A, 51, 511

Levi, M., Bebek, C., Beers, T., et al. 2013, arXiv:1308.0847

López, S., D'Odorico, V., Ellison, S. L., et al. 2016, A&A, 594, A91

MacLeod, C. L., Ivezić, Ž., Sesar, B., et al. 2012, ApJ, 753, 106

Maiolino, R., Gallerani, S., Neri, R., et al. 2012, MNRAS, 425, L66

Mason, R. E., Rodríguez-Ardila, A., Martins, L., et al. 2015, ApJS, 217, 13

McConnell, N. J., & Ma, C.-P. 2013, ApJ, 764, 184

McIntosh, D. H., Rieke, M. J., Rix, H.-W., et al. 1999, ApJ, 514, 40

Mejía-Restrepo, J. E., Trakhtenbrot, B., Lira, P., et al. 2016, MNRAS, 460, 187

Merloni, A., Bongiorno, A., Bolzonella, M., et al. 2010, ApJ, 708, 137

Meusinger, H., Schalldach, P., Mirhosseini, A., et al. 2016, A&A, 587, A83

Netzer, H. 2003, ApJL, 583, L5

Netzer, H., Shemmer, O., Maiolino, R., et al. 2004, ApJ, 614, 558

Netzer, H., Lira, P., Trakhtenbrot, B., et al. 2007, ApJ, 671, 1256

Pâris, I., Petitjean, P., Ross, N. P., et al. 2017, A&A, 597, A79

12

Pâris, I., Petitjean, P., Aubourg, É., et al. 2018, A&A, 613, A51

Rafiee, A., Pirkola, P., Hall, P. B., et al. 2016, MNRAS, 459, 2472

Reines, A. E., & Volonteri, M. 2015, ApJ, 813, 82

Richards, G. T., Fan, X., Newberg, H. J., et al. 2002, AJ, 123, 2945

Richards, G. T., Strauss, M. A., Fan, X., et al. 2006, AJ, 131, 2766

Richards, G. T., Kruczek, N. E., Gallagher, S. C., et al. 2011, AJ, 141, 167

Robberto, M., Roming, P. W., van der Horst, A. J., et al. 2018, Proc. SPIE, 107020I

Shemmer, O., Netzer, H., Maiolino, R., et al. 2004, ApJ, 614, 547

Shen, Y., Richards, G. T., Strauss, M. A., et al. 2011, ApJS, 194, 45

Shen, Y., & Liu, X. 2012, ApJ, 753, 125

Shen, Y., Liu, X., Loeb, A., et al. 2013, ApJ, 775, 49

Shen, Y. 2016, ApJ, 817, 55

Shen, Y., Brandt, W. N., Richards, G. T., et al. 2016, ApJ, 831, 7

Shen, Y., Hall, P. B., Horne, K., et al. 2019, ApJS, 241, 34

Shen, Y., Wu, J., Jiang, L., et al. 2019, ApJ, 873, 35

Skrutskie, M. F., Cutri, R. M., Stiening, R., et al. 2006, AJ, 131, 1163

Spergel, D. N., Bean, R., Doré, O., et al. 2007, ApJS, 170, 377

Stern, D., Graham, M. J., Arav, N., et al. 2017, ApJ, 839, 106

Storey, P. J. & Zeippen, C. J. 2000, MNRAS, 312, 813

Sulentic, J. W., Stirpe, G. M., Marziani, P., et al. 2004, A&A, 423, 121

Trakhtenbrot, B., Netzer, H., Lira, P., et al. 2011, ApJ, 730, 7

Trakhtenbrot, B., & Netzer, H. 2012, MNRAS, 427, 3081

Vanden Berk, D. E., Richards, G. T., Bauer, A., et al. 2001, AJ, 122, 549

Vanden Berk, D. E., Wilhite, B. C., Kron, R. G., et al. 2004, ApJ, 601, 692

Vestergaard, M., & Wilkes, B. J. 2001, ApJS, 134, 1

Wills, B. J. & Browne, I. W. A. 1986, ApJ, 302, 56

Wills, B. J., Laor, A., Brotherton, M. S., et al. 1999, ApJL, 515, L53

Woo, J.-H., Treu, T., Barth, A. J., et al. 2010, ApJ, 716, 269

Wu, J., Brandt, W. N., Anderson, S. F., et al. 2012, ApJ, 747, 10

York, D. G., Adelman, J., Anderson, J. E., et al. 2000, AJ, 120, 1579

Zuo, W., Wu, X.-B., Fan, X., et al. 2015, ApJ, 799, 189

Table 1. Observation Log

Quasar	z_{SDSS}[a]	J	H	K	Obs. Date	Semester	Net Exp.	Comments	BAL	RL
		[mag]	[mag]	[mag]			[s]			
(1)	(2)	(3)	(4)	(5)	(6)	(7)	(8)	(9)	(10)	(11)
SDSS J000544.71−044915.2	2.322	16.94	16.09	16.66	2019 Oct 18	2019B	1800	4	⋯	⋯
SDSS J000730.94−095831.5	2.223	17.09	15.94	15.37	2019 Jan 06	2018B	1800	4	1	⋯
SDSS J001249.89+285552.6	3.236	16.51	15.71	15.49	2017 Sep 09	2017B	1800	⋯	1	⋯
SDSS J001355.10−012304.0	3.396	16.71	16.05	15.46	2019 Jan 05	2018B	900	⋯	1	⋯
	⋯	⋯	⋯	⋯	2019 Jan 07	2018B	900	⋯	⋯	⋯
SDSS J001453.20+091217.6	2.338	16.65	15.92	15.14	2017 Sep 19	2017B	2025	1	⋯	⋯
SDSS J001813.30+361058.6	2.316	16.15	15.65	14.75	2017 Aug 31	2017B	1800	⋯	⋯	⋯
SDSS J001914.46+155555.9	2.271	16.72	15.81	15.14	2017 Sep 01	2017B	1800	⋯	⋯	⋯
SDSS J002634.46+274015.5	2.250	17.05	15.92	15.25	2018 Dec 20	2018B	1800	⋯	⋯	⋯
SDSS J003416.61+002241.1	1.632	16.48	15.86	15.68	2017 Sep 01	2017B	1800	⋯	⋯	⋯
SDSS J004300.26+045718.6	2.362	16.22	15.65	14.89	2018 Dec 21	2018B	1800	4	1	⋯
SDSS J004719.71+014813.9	1.590	16.57	16.06	15.25	2018 Dec 24	2018B	1800	⋯	⋯	⋯
SDSS J005233.67+014040.8	2.301	15.99	15.22	14.59	2019 Jul 04	2019B	900	⋯	⋯	⋯
SDSS J005408.29+020751.6	1.590	16.53	15.90	15.50	2018 Nov 25	2018B	2250	1,4	1	⋯
SDSS J010113.72+032427.0	1.579	16.23	15.38	15.25	2018 Dec 21	2018B	1800	⋯	⋯	1
SDSS J010328.72−110414.4	2.195	16.90	15.86	15.47	2017 Sep 04	2017B	1800	⋯	⋯	1
SDSS J010447.39+101031.6	2.361	17.36	16.07	15.46	2019 Oct 18	2019B	1800	⋯	⋯	1
SDSS J010500.72+194230.4	2.320	16.73	15.76	15.00	2017 Sep 04	2017B	1800	⋯	⋯	⋯
SDSS J010615.93+101043.0	2.350	17.09	16.09	15.30	2019 Nov 26	2019B	1920	⋯	⋯	⋯
SDSS J010643.23−031536.4	2.242	16.58	15.75	15.19	2018 Dec 24	2018B	1800	⋯	⋯	⋯
SDSS J011218.07+353011.7	2.305	17.06	16.04	15.69	2019 Nov 29	2019B	1800	4	1	⋯
SDSS J011515.84+110651.1	2.280	16.92	16.01	14.94	2019 Nov 29	2019B	1800	4	⋯	⋯
SDSS J011538.72+242446.0	2.374	16.55	15.74	15.09	2019 Jan 06	2018B	1800	⋯	⋯	⋯
SDSS J013012.36+153157.9	2.349	16.43	15.82	14.71	2017 Sep 04	2017B	1800	⋯	1	⋯
SDSS J013113.25+085245.5	3.532	16.63	16.16	15.32	2017 Sep 01	2017B	1800	⋯	⋯	⋯
SDSS J013136.44+130331.0	1.594	16.29	15.43	15.61	2018 Aug 30	2018B	2025	1	⋯	⋯
SDSS J013417.81−005036.2	2.254	16.64	15.85	15.16	2018 Dec 24	2018B	1800	⋯	⋯	⋯
SDSS J013647.96−062753.6	3.285	16.46	16.03	15.47	2018 Nov 25	2018B	1800	⋯	⋯	⋯
SDSS J013652.52+122501.5	2.393	16.64	15.78	14.73	2017 Oct 29	2017B	1800	⋯	1	1
SDSS J014018.20−013805.8	2.235	16.10	15.42	14.58	2018 Nov 25	2018B	900	⋯	1	⋯
SDSS J014128.26+070606.1	2.265	17.01	16.08	15.24	2019 Nov 26	2019B	1920	1	⋯	⋯
	⋯	⋯	⋯	⋯	2019 Nov 29	2019B	1920	⋯	⋯	⋯
SDSS J014206.86+025713.0	2.315	15.75	14.92	13.99	2018 Nov 26	2018B	900	⋯	1	⋯
SDSS J014932.06+152754.0	2.389	16.82	16.06	15.29	2019 Nov 27	2019B	1920	⋯	⋯	⋯
SDSS J021259.21+132618.8	1.619	16.49	15.67	15.59	2017 Sep 25	2017B	1800	3	⋯	⋯
SDSS J022007.64−010731.1	3.441	16.90	16.19	15.36	2017 Sep 01	2017B	1800	⋯	1	⋯
SDSS J024318.99+025746.6	3.280	16.47	15.92	15.68	2019 Dec 04	2019B	1800	4	1	⋯
SDSS J025042.45+003536.7	2.387	16.72	15.77	15.25	2017 Sep 09	2017B	1800	⋯	1	⋯
SDSS J035150.97−061326.4	2.221	16.21	15.74	15.17	2017 Oct 30	2017B	1800	⋯	⋯	⋯
SDSS J072517.52+434553.4	1.594	16.14	15.50	15.01	2017 Oct 20	2017B	1880	1	⋯	⋯
SDSS J072928.48+252451.8	2.306	16.67	15.67	14.95	2017 Nov 05	2017B	1800	⋯	⋯	⋯
SDSS J073519.68+240104.6	3.278	16.81	16.45	15.35	2017 Sep 21	2017B	1800	⋯	1	⋯
SDSS J073900.90+485159.0	1.620	16.62	15.81	15.63	2018 Dec 23	2018B	1800	⋯	⋯	⋯
SDSS J073913.65+461858.5	1.581	16.22	15.71	15.22	2018 Dec 17	2018B	1800	⋯	⋯	⋯
SDSS J074941.16+262715.9	1.592	16.53	15.60	15.35	2017 Nov 06	2017B	1800	⋯	⋯	⋯
SDSS J075115.43+505439.1	2.300	15.89	15.55	14.90	2019 Oct 02	2019B	1800	⋯	⋯	⋯
SDSS J075136.36+432732.4	2.250	16.67	15.75	15.22	2018 Dec 17	2018B	1800	⋯	⋯	⋯
SDSS J075405.08+280339.6	2.271	16.49	15.96	15.27	2018 Dec 24	2018B	1800	⋯	⋯	⋯
SDSS J075547.83+220450.1	2.314	16.08	15.50	14.74	2017 Nov 02	2017B	1880	⋯	⋯	⋯

Table 1 continued

Table 1 *(continued)*

Quasar	$z_{\rm SDSS}$[a]	J	H	K	Obs. Date	Semester	Net Exp.	Comments	BAL	RL
		[mag]	[mag]	[mag]			[s]			
(1)	(2)	(3)	(4)	(5)	(6)	(7)	(8)	(9)	(10)	(11)
SDSS J075837.62+135733.7	2.198	16.37	15.56	14.48	2018 Dec 20	2018B	1800	$\cdots$	$\cdots$	1
SDSS J080036.01+501044.3	1.621	15.84	15.41	15.12	2017 Nov 04	2017B	940	$\cdots$	$\cdots$	1
SDSS J080117.79+521034.5	3.209	15.71	15.34	14.61	2017 Nov 04	2017B	1880	$\cdots$	$\cdots$	$\cdots$
SDSS J080413.66+251633.9	2.298	16.27	15.68	14.89	2019 Jan 03	2018B	1800	$\cdots$	$\cdots$	1
SDSS J080937.55+263729.6	2.260	16.69	16.02	15.61	2019 Oct 27	2019B	1800	4	$\cdots$	$\cdots$
SDSS J081019.47+095040.9	2.218	16.58	15.87	15.06	2017 Dec 29	2017B	1800	$\cdots$	$\cdots$	$\cdots$
SDSS J081056.96+120914.8	2.259	16.16	15.45	14.68	2017 Dec 29	2017B	1410	1	$\cdots$	$\cdots$
SDSS J081114.66+172057.4	2.323	16.19	15.49	14.65	2017 Nov 04	2017B	940	$\cdots$	1	$\cdots$
SDSS J081127.44+461812.9	2.257	15.96	15.64	14.88	2017 Nov 14	2017B	1880	$\cdots$	$\cdots$	$\cdots$
SDSS J081342.09+344235.3	2.245	17.14	16.01	15.23	2019 Oct 27	2019B	1800	4	1	$\cdots$
SDSS J081410.76+443706.9	2.277	16.83	16.03	15.11	2019 Dec 04	2019B	2250	$\cdots$	$\cdots$	$\cdots$
SDSS J081558.35+154055.2	2.230	16.39	15.63	14.90	2019 Jan 03	2018B	1800	$\cdots$	$\cdots$	$\cdots$
SDSS J081940.58+082357.9	3.204	16.80	15.80	15.70	2019 Oct 27	2019B	1800	$\cdots$	$\cdots$	$\cdots$
SDSS J082507.67+360411.1	1.579	15.52	14.79	14.75	2017 Dec 30	2017B	940	3	$\cdots$	$\cdots$
SDSS J082603.32+342800.6	2.307	16.50	15.80	15.17	2018 Dec 20	2018B	1800	$\cdots$	$\cdots$	$\cdots$
SDSS J082613.85+495019.3	2.180	16.49	16.08	15.27	2019 Dec 09	2019B	1880	4	$\cdots$	$\cdots$
SDSS J082643.45+143427.6	2.308	16.88	16.00	15.63	2019 Nov 16	2019B	1800	$\cdots$	$\cdots$	1
SDSS J082644.66+163549.0	2.189	15.89	15.32	14.28	2018 Nov 25	2018B	1125	1	$\cdots$	$\cdots$
SDSS J082736.89+061812.1	2.192	15.99	15.19	14.21	2018 Nov 20	2018B	900	1	$\cdots$	$\cdots$
	$\cdots$	$\cdots$	$\cdots$	$\cdots$	2018 Dec 23	2018B	900	$\cdots$	$\cdots$	$\cdots$
SDSS J082852.67−042938.9	2.275	16.70	16.07	15.41	2019 Dec 11	2019B	1800	4	1	$\cdots$
SDSS J083255.63+182300.7	2.274	15.90	15.43	14.68	2018 Dec 20	2018B	900	$\cdots$	$\cdots$	$\cdots$
SDSS J083417.12+354833.1	2.163	15.71	15.29	14.60	2017 Nov 13	2017B	940	$\cdots$	$\cdots$	$\cdots$
SDSS J083745.74+052109.4	2.355	16.43	15.85	15.15	2019 Jan 11	2018B	1800	$\cdots$	1	$\cdots$
SDSS J084029.97+465113.7	1.572	15.90	15.20	15.03	2017 Nov 10	2017B	940	$\cdots$	$\cdots$	$\cdots$
SDSS J084133.15+200525.7	2.342	15.09	14.41	13.62	2019 Feb 03	2019A	900	1	1	$\cdots$
SDSS J084526.75+550546.8	1.618	16.33	15.65	15.18	2018 Jan 05	2017B	1800	1,4	$\cdots$	$\cdots$
SDSS J084729.52+441616.7	2.347	16.61	15.51	15.01	2019 Jan 03	2018B	1800	$\cdots$	1	$\cdots$
SDSS J084846.11+611234.6	2.258	15.38	14.73	13.89	2017 Nov 02	2017B	640	$\cdots$	$\cdots$	$\cdots$
SDSS J085046.17+522057.4	2.230	15.94	15.45	14.55	2019 Sep 30	2019B	900	$\cdots$	1	$\cdots$
SDSS J085337.36+121800.3	2.196	16.06	15.65	14.80	2017 Dec 30	2017B	2350	1	$\cdots$	$\cdots$
SDSS J085344.17+354104.5	2.175	16.79	16.02	15.30	2019 Oct 27	2019B	1800	$\cdots$	$\cdots$	$\cdots$
SDSS J085443.10+075223.2	1.604	16.62	15.62	15.51	2019 Jan 21	2019A	1800	$\cdots$	$\cdots$	$\cdots$
SDSS J085726.94+331317.1	2.339	16.26	15.60	15.19	2019 Jan 01	2018B	1800	$\cdots$	$\cdots$	1
SDSS J085856.00+015219.4	2.172	16.87	15.78	15.06	2018 Jan 02	2017B	1800	3	$\cdots$	$\cdots$
SDSS J085946.79+603702.1	2.276	16.71	15.97	15.11	2019 Nov 16	2019B	450	$\cdots$	$\cdots$	$\cdots$
	$\cdots$	$\cdots$	$\cdots$	$\cdots$	2019 Dec 11	2019B	1800	$\cdots$	$\cdots$	$\cdots$
SDSS J090247.57+304120.7	1.560	15.74	15.08	14.89	2017 Oct 20	2017B	940	$\cdots$	$\cdots$	$\cdots$
SDSS J090444.33+233354.0	2.259	15.77	15.25	14.21	2018 Jan 02	2017B	940	$\cdots$	$\cdots$	1
SDSS J090646.98+174046.8	1.579	16.25	15.47	15.20	2019 Jan 01	2018B	1800	$\cdots$	$\cdots$	$\cdots$
SDSS J090709.89+250620.8	3.310	16.24	15.71	15.08	2018 Dec 21	2018B	1800	$\cdots$	$\cdots$	$\cdots$
SDSS J090710.36+430000.2	2.189	15.88	15.41	14.67	2018 Jan 05	2017B	940	3	$\cdots$	$\cdots$
SDSS J091000.56+401158.5	2.176	16.81	16.06	15.36	2019 Dec 11	2019B	1920	4	$\cdots$	$\cdots$
SDSS J091054.17+375914.9	2.162	16.45	15.85	15.12	2019 Mar 16	2019A	1800	3	$\cdots$	1
SDSS J091118.02+202254.7	3.225	16.96	16.08	15.30	2017 Nov 03	2017B	1305	3	$\cdots$	1
SDSS J091301.01+422344.7	2.315	16.07	15.50	14.43	2018 Jan 02	2017B	1880	$\cdots$	1	$\cdots$
SDSS J091328.22+394443.9	1.582	16.40	15.85	15.32	2018 Jan 01	2017B	1800	$\cdots$	1	1
SDSS J091716.79+461435.4	1.626	16.33	15.61	15.33	2018 Jan 05	2017B	1800	3	1	$\cdots$
SDSS J091941.26+253537.7	2.267	16.81	16.02	15.96	2019 Dec 10	2019B	1800	$\cdots$	$\cdots$	$\cdots$
SDSS J092216.04+160526.4	2.373	16.47	15.94	15.05	2017 Dec 29	2017B	1800	$\cdots$	$\cdots$	$\cdots$
SDSS J092325.25+453222.2	3.452	16.44	16.02	15.64	2019 Dec 10	2019B	1800	$\cdots$	$\cdots$	$\cdots$

Table 1 continued

Table 1 *(continued)*

Quasar	z_{SDSS}[a]	J	H	K	Obs. Date	Semester	Net Exp.	Comments	BAL	RL
		[mag]	[mag]	[mag]			[s]			
(1)	(2)	(3)	(4)	(5)	(6)	(7)	(8)	(9)	(10)	(11)
SDSS J092456.66+305354.7	3.457	16.39	16.04	15.33	2019 Jun 19	2019A	1800	$\cdots$	$\cdots$	$\cdots$
	$\cdots$	$\cdots$	$\cdots$	$\cdots$	2019 Dec 10	2019B	1800	$\cdots$	$\cdots$	$\cdots$
SDSS J092523.24+214119.8	2.364	16.66	15.79	15.13	2019 Jan 03	2018B	1800	$\cdots$	$\cdots$	$\cdots$
SDSS J092555.05+490338.2	2.343	16.77	16.01	15.50	2019 Dec 11	2019B	1800	$\cdots$	$\cdots$	$\cdots$
SDSS J093251.98+023727.0	2.165	16.85	15.85	15.28	2018 Dec 21	2018B	1800	$\cdots$	1	$\cdots$
SDSS J093533.88+235720.5	2.306	16.67	15.93	15.29	2019 Jan 09	2018B	1800	$\cdots$	$\cdots$	$\cdots$
SDSS J093952.61+195838.3	1.580	15.81	15.00	14.85	2018 Jan 06	2017B	1880	4	1	$\cdots$
SDSS J094140.16+325703.2	3.453	16.55	15.81	15.24	2018 Jan 06	2017B	1800	4	$\cdots$	$\cdots$
SDSS J094214.40+034100.3	1.583	16.62	15.99	15.53	2019 Dec 16	2019B	1880	$\cdots$	$\cdots$	$\cdots$
SDSS J094328.94+140415.6	2.400	16.63	15.86	14.88	2018 Jan 03	2017B	900	1	1	$\cdots$
	$\cdots$	$\cdots$	$\cdots$	$\cdots$	2018 Jan 06	2017B	900	$\cdots$	$\cdots$	$\cdots$
SDSS J094347.02+690818.4	1.598	16.62	15.74	15.68	2019 Jan 03	2018B	1800	$\cdots$	$\cdots$	$\cdots$
SDSS J094427.27+614424.6	2.333	16.41	15.61	14.72	2019 Dec 12	2019B	2250	$\cdots$	1	$\cdots$
SDSS J094602.31+274407.0	2.440	15.87	15.28	14.55	2017 Nov 10	2017B	940	$\cdots$	$\cdots$	1
SDSS J094637.83−012411.5	2.214	16.99	15.72	15.34	2017 Nov 13	2017B	1800	$\cdots$	$\cdots$	$\cdots$
SDSS J094646.94+392719.0	2.220	16.70	16.08	15.57	2019 Oct 24	2019B	1920	$\cdots$	$\cdots$	$\cdots$
SDSS J094648.59+171827.7	2.294	16.90	15.87	15.01	2019 Mar 09	2019A	1800	$\cdots$	$\cdots$	$\cdots$
SDSS J094902.38+531241.5	1.611	16.61	16.07	15.96	2019 Jan 01	2018B	1800	$\cdots$	1	$\cdots$
SDSS J095058.76+263424.6	2.401	16.61	15.94	15.64	2018 Dec 19	2018B	1800	$\cdots$	$\cdots$	$\cdots$
SDSS J095327.95+322551.6	1.575	16.13	15.28	14.81	2019 Feb 06	2019A	1800	$\cdots$	$\cdots$	1
SDSS J095330.36+353223.1	2.385	16.93	15.90	15.69	2018 Dec 17	2018B	1800	$\cdots$	$\cdots$	$\cdots$
SDSS J095544.26+182546.9	3.482	16.80	15.83	15.58	2019 Jan 10	2018B	1800	$\cdots$	$\cdots$	$\cdots$
SDSS J095707.82+184739.9	2.380	16.54	15.68	15.37	2018 Jan 03	2017B	1800	$\cdots$	$\cdots$	$\cdots$
SDSS J095746.75+565800.7	1.575	16.08	15.31	15.04	2017 Nov 03	2017B	900	1,3	1	$\cdots$
	$\cdots$	$\cdots$	$\cdots$	$\cdots$	2018 Jan 04	2017B	900	$\cdots$	$\cdots$	$\cdots$
SDSS J095823.07+371218.3	2.280	16.33	15.81	15.33	2018 Jan 02	2017B	1800	$\cdots$	$\cdots$	$\cdots$
SDSS J095852.19+120245.0	3.298	16.29	15.70	14.98	2018 Jan 02	2017B	940	$\cdots$	$\cdots$	$\cdots$
SDSS J100212.63+520800.2	1.613	16.52	15.96	15.98	2019 Jan 03	2018B	1800	$\cdots$	$\cdots$	$\cdots$
SDSS J100610.55+370513.8	3.204	16.30	15.69	15.27	2017 Nov 04	2017B	940	$\cdots$	1	$\cdots$
	$\cdots$	$\cdots$	$\cdots$	$\cdots$	2017 Nov 10	2017B	940	$\cdots$	$\cdots$	$\cdots$
SDSS J100653.26+011938.7	2.298	16.80	15.92	15.20	2019 Jan 10	2018B	1800	$\cdots$	1	$\cdots$
SDSS J100850.06−023831.6	2.259	17.05	15.92	15.50	2019 Jan 03	2018B	1800	$\cdots$	$\cdots$	$\cdots$
SDSS J101106.74+114759.4	2.248	17.03	15.87	15.04	2019 Jan 02	2018B	1800	$\cdots$	$\cdots$	$\cdots$
SDSS J101211.44+330926.4	2.254	16.59	15.85	15.17	2017 Dec 04	2017B	1350	$\cdots$	$\cdots$	1
	$\cdots$	$\cdots$	$\cdots$	$\cdots$	2018 Jan 03	2017B	900	$\cdots$	$\cdots$	$\cdots$
SDSS J101353.43+244916.4	1.634	15.03	14.06	13.90	2018 Jan 02	2017B	640	$\cdots$	$\cdots$	1
SDSS J101425.11+032003.7	2.146	16.61	15.82	15.17	2018 Jan 03	2017B	1800	$\cdots$	$\cdots$	$\cdots$
SDSS J101429.57+481938.4	1.571	16.25	15.53	15.32	2018 Jan 03	2017B	1800	$\cdots$	$\cdots$	$\cdots$
SDSS J101542.04+430455.6	2.425	16.49	16.05	15.34	2019 Dec 18	2019B	1800	$\cdots$	1	$\cdots$
SDSS J101724.26+333403.3	1.573	16.49	15.84	15.40	2018 Jan 03	2017B	1800	1,4	$\cdots$	$\cdots$
SDSS J101921.62+354036.7	1.557	16.24	15.66	15.77	2017 Nov 03	2017B	1305	4	$\cdots$	$\cdots$
SDSS J102154.00+051646.3	3.439	16.75	16.06	15.33	2018 Dec 16	2018B	1800	$\cdots$	1	$\cdots$
SDSS J102537.69+211509.1	2.252	16.30	15.90	14.89	2018 Dec 19	2018B	1800	3	$\cdots$	$\cdots$
SDSS J102648.15+295410.9	2.335	16.61	15.54	15.09	2018 Jan 02	2017B	940	4	$\cdots$	$\cdots$
SDSS J102731.49+541809.7	1.593	16.55	15.72	15.71	2019 Jan 04	2018B	900	$\cdots$	$\cdots$	$\cdots$
	$\cdots$	$\cdots$	$\cdots$	$\cdots$	2019 Jan 13	2018B	900	$\cdots$	$\cdots$	$\cdots$
SDSS J102907.09+651024.6	2.175	15.88	15.41	14.57	2018 Mar 29	2018A	920	$\cdots$	$\cdots$	$\cdots$
SDSS J103209.78+385630.6	1.584	16.21	15.86	15.49	2019 Apr 15	2019A	1800	$\cdots$	$\cdots$	$\cdots$
SDSS J103236.98+230554.1	2.379	16.99	16.09	15.41	2019 Dec 16	2019B	1920	$\cdots$	$\cdots$	$\cdots$
SDSS J103246.19+323618.0	2.380	17.02	15.90	15.41	2019 Dec 16	2019B	1800	$\cdots$	1	$\cdots$
SDSS J103405.73+463545.4	2.215	16.74	15.96	15.13	2018 Jan 08	2018B	1800	$\cdots$	1	$\cdots$

Table 1 continued

Table 1 *(continued)*

Quasar	$z_{\rm SDSS}$[a]	J	H	K	Obs. Date	Semester	Net Exp.	Comments	BAL	RL
		[mag]	[mag]	[mag]			[s]			
(1)	(2)	(3)	(4)	(5)	(6)	(7)	(8)	(9)	(10)	(11)
SDSS J103546.02+110546.4	2.359	15.70	15.13	14.23	2017 Nov 17	2017B	940	4	$\cdots$	$\cdots$
SDSS J103718.23+302509.1	2.293	16.94	15.69	15.57	2019 Mar 03	2019A	1350	1	1	$\cdots$
SDSS J104018.51+572448.1	3.411	16.96	15.97	15.30	2019 Jan 01	2018B	1800	$\cdots$	$\cdots$	1
SDSS J104330.09+441051.5	2.215	16.63	15.76	15.52	2018 Dec 19	2018B	1800	$\cdots$	$\cdots$	$\cdots$
SDSS J104336.73+494707.6	2.194	16.34	15.78	14.78	2018 Dec 20	2018B	1800	$\cdots$	$\cdots$	$\cdots$
SDSS J104621.57+483322.6	1.577	16.38	16.06	15.52	2019 Jan 07	2018B	1800	$\cdots$	1	$\cdots$
SDSS J104716.50+360654.0	2.291	16.68	15.88	15.25	2018 Dec 21	2018B	1800	$\cdots$	$\cdots$	1
SDSS J104743.57+661830.5	2.171	16.43	15.64	15.20	2019 Jan 03	2018B	1800	$\cdots$	$\cdots$	$\cdots$
SDSS J104911.34+495113.6	1.606	15.40	14.58	14.28	2017 Oct 28	2017B	640	$\cdots$	$\cdots$	$\cdots$
SDSS J104941.58+522348.9	2.384	17.01	15.91	15.27	2019 Dec 12	2019B	1800	$\cdots$	1	$\cdots$
SDSS J105045.72+544719.2	2.173	15.85	15.38	14.45	2019 Mar 09	2019A	920	$\cdots$	$\cdots$	$\cdots$
SDSS J105714.82+440323.8	3.340	16.14	15.70	15.01	2019 Feb 03	2019A	470	4	$\cdots$	$\cdots$
SDSS J105902.04+580848.6	2.248	16.61	15.93	15.00	2019 Jan 03	2018B	900	$\cdots$	$\cdots$	$\cdots$
SDSS J105926.43+062227.4	2.199	16.00	15.27	14.71	2019 Mar 17	2019A	920	$\cdots$	$\cdots$	$\cdots$
SDSS J110148.85+054815.5	1.589	16.22	15.52	15.33	2019 Dec 12	2019B	1800	$\cdots$	1	$\cdots$
SDSS J110516.68+200013.7	2.362	16.31	15.67	15.08	2019 Apr 15	2019A	1800	$\cdots$	$\cdots$	$\cdots$
SDSS J110735.58+642008.6	2.330	16.21	15.74	15.08	2019 Dec 27	2019B	1800	$\cdots$	$\cdots$	$\cdots$
SDSS J110810.87+014140.7	1.614	16.34	15.72	15.61	2019 Dec 28	2019B	1800	$\cdots$	$\cdots$	$\cdots$
SDSS J111119.10+133603.8	3.475	15.89	15.51	15.03	2019 Mar 17	2019A	940	3	$\cdots$	$\cdots$
SDSS J111313.29+102212.4	2.261	16.02	15.48	14.62	2019 Jun 16	2019A	1800	$\cdots$	1	$\cdots$
SDSS J111352.53+104041.9	1.603	16.47	15.61	15.22	2019 Dec 29	2019B	1800	$\cdots$	1	$\cdots$
SDSS J111850.02+351311.7	2.175	16.47	15.77	15.32	2019 May 13	2019A	1800	$\cdots$	$\cdots$	$\cdots$
SDSS J111920.98+232539.4	2.289	16.68	15.86	15.18	2019 Dec 29	2019B	1800	$\cdots$	1	$\cdots$
SDSS J112127.79+254758.9	1.587	16.26	15.41	15.38	2019 May 18	2019A	1800	$\cdots$	1	$\cdots$
SDSS J113048.45+225206.6	2.370	16.86	16.01	15.12	2020 Feb 04	2020A	1800	$\cdots$	1	1
SDSS J113621.04+005021.2	3.428	16.45	15.81	15.48	2019 Mar 17	2019A	1800	$\cdots$	$\cdots$	$\cdots$
SDSS J113740.61+630256.9	2.322	16.47	15.81	14.85	2019 Dec 16	2019B	1800	$\cdots$	1	$\cdots$
SDSS J113924.64+332436.9	2.314	16.38	15.95	14.85	2020 Mar 06	2020A	1800	$\cdots$	1	$\cdots$
SDSS J114212.25+233250.5	1.600	16.09	15.52	15.14	2020 Jan 04	2019B	1800	$\cdots$	$\cdots$	$\cdots$
SDSS J114323.71+193448.0	3.348	16.10	15.72	15.31	2019 Mar 17	2019A	1800	$\cdots$	1	$\cdots$
SDSS J114350.30+362911.3	2.343	16.19	15.51	15.14	2019 Jun 18	2019A	1800	$\cdots$	$\cdots$	$\cdots$
SDSS J114705.24+083900.6	1.604	16.08	15.18	14.79	2019 Nov 15	2019B	900	$\cdots$	1	1
SDSS J114711.78+084029.6	2.333	16.64	15.79	15.21	2019 Jun 14	2019A	1800	$\cdots$	$\cdots$	$\cdots$
SDSS J114738.35+301717.5	3.353	16.80	16.09	15.42	2019 Jun 17	2019A	1800	$\cdots$	1	$\cdots$
	$\cdots$	$\cdots$	$\cdots$	$\cdots$	2019 Dec 30	2019B	1920	$\cdots$	$\cdots$	$\cdots$
SDSS J114902.70+144328.0	2.190	16.36	15.88	14.95	2019 Jun 14	2019A	1800	$\cdots$	$\cdots$	$\cdots$
SDSS J114907.15+004104.3	2.301	16.85	15.47	14.95	2019 Jun 18	2019A	1800	$\cdots$	$\cdots$	$\cdots$
SDSS J114927.90+432727.9	3.305	16.86	15.91	15.38	2019 Dec 18	2019B	1800	$\cdots$	$\cdots$	$\cdots$
SDSS J115034.53+653928.2	2.224	15.32	14.82	14.08	2019 Mar 17	2019A	628	4	$\cdots$	$\cdots$
SDSS J115747.99+272459.6	2.206	16.14	15.43	14.48	2019 Jun 17	2019A	2025	$\cdots$	1	$\cdots$
SDSS J120452.82+354007.4	1.592	16.56	15.92	15.89	2019 Mar 01	2019A	1800	4	1	$\cdots$
SDSS J121314.03+080703.6	2.376	16.63	15.88	15.30	2019 May 23	2019A	1800	$\cdots$	$\cdots$	$\cdots$
SDSS J121404.11+330945.6	1.595	16.16	15.46	15.15	2019 Dec 28	2019B	900	$\cdots$	$\cdots$	$\cdots$
SDSS J121423.01+024252.8	2.231	16.32	15.76	15.15	2019 Jun 13	2019A	1800	$\cdots$	$\cdots$	1
SDSS J121519.42+424851.0	2.314	16.45	15.80	14.50	2019 Feb 26	2019A	1800	3	$\cdots$	$\cdots$
SDSS J121736.65+515510.3	2.225	16.04	15.39	14.44	2019 Jun 16	2019A	1800	$\cdots$	$\cdots$	1
SDSS J121810.98+241410.9	2.381	15.78	15.13	14.33	2019 Mar 18	2019A	920	$\cdots$	$\cdots$	$\cdots$
SDSS J121843.39+153617.2	2.268	15.27	14.52	13.83	2019 Mar 08	2019A	600	4	$\cdots$	$\cdots$
SDSS J121940.36$-$010007.4	1.575	15.60	15.06	14.84	2019 Mar 19	2019A	920	4	$\cdots$	$\cdots$
SDSS J122046.05+455442.1	2.220	15.71	15.07	14.23	2018 Jun 23	2018A	920	$\cdots$	$\cdots$	$\cdots$
SDSS J122709.48+310749.3	2.190	16.57	15.59	14.93	2019 May 24	2019A	1800	$\cdots$	$\cdots$	$\cdots$

Table 1 continued

Table 1 *(continued)*

Quasar	$z_{\rm SDSS}$[a]	J	H	K	Obs. Date	Semester	Net Exp.	Comments	BAL	RL
		[mag]	[mag]	[mag]			[s]			
(1)	(2)	(3)	(4)	(5)	(6)	(7)	(8)	(9)	(10)	(11)
SDSS J123514.64+462904.0	2.204	16.43	15.86	14.90	2019 May 22	2019A	1800	$\cdots$	$\cdots$	$\cdots$
SDSS J124512.86+194727.5	2.173	15.95	15.26	14.73	2019 Jul 14	2019B	900	4	$\cdots$	$\cdots$
SDSS J125150.45+114340.7	2.195	16.46	15.70	14.83	2019 Apr 20	2019A	1800	3	$\cdots$	$\cdots$
SDSS J125159.90+500203.6	2.385	16.43	15.70	15.40	2019 Dec 12	2019B	1800	$\cdots$	$\cdots$	$\cdots$
SDSS J132736.56+033128.3	1.594	15.61	14.87	14.84	2020 Jul 08	2020A	1200	4	1	$\cdots$
SDSS J133342.56+123352.7	3.275	16.60	15.80	15.18	2019 May 18	2019A	1800	$\cdots$	1	$\cdots$
SDSS J133448.87+515743.6	3.240	16.77	16.04	15.62	2020 Jul 08	2020A	1800	4	1	$\cdots$
SDSS J134341.99+255652.9	1.600	15.77	15.00	14.63	2019 Mar 19	2019A	1380	3	$\cdots$	$\cdots$
SDSS J135827.12+170510.3	2.233	16.71	15.82	14.96	2019 Mar 23	2019A	1800	4	$\cdots$	$\cdots$
SDSS J135908.35+305830.8	2.290	16.19	15.63	14.93	2019 May 14	2019A	1800	3	$\cdots$	$\cdots$
SDSS J140058.79+260619.4	2.351	16.43	15.70	14.95	2018 Jun 26	2018A	1800	$\cdots$	1	$\cdots$
SDSS J140704.43+273556.6	2.225	16.46	15.98	14.86	2020 Jun 30	2020A	1800	$\cdots$	$\cdots$	$\cdots$
SDSS J141028.14+135950.2	2.213	16.21	15.52	14.67	2019 Mar 09	2019A	900	1,3	$\cdots$	$\cdots$
	$\cdots$	$\cdots$	$\cdots$	$\cdots$	2019 Mar 23	2019A	900	$\cdots$	$\cdots$	$\cdots$
SDSS J141617.38+264906.1	2.299	16.39	15.68	14.84	2019 May 22	2019A	1800	$\cdots$	$\cdots$	1
SDSS J141925.48+074953.5	2.394	16.37	15.69	14.86	2019 May 19	2019A	1800	$\cdots$	$\cdots$	$\cdots$
SDSS J141951.84+470901.3	2.296	15.72	15.05	14.30	2019 May 14	2019A	1800	3	$\cdots$	$\cdots$
SDSS J142013.03+253403.9	2.235	16.34	15.67	15.03	2019 Apr 17	2019A	1800	$\cdots$	1	$\cdots$
SDSS J142330.09+115951.2	1.613	16.22	15.43	15.27	2019 Mar 23	2019A	1800	4	$\cdots$	1
SDSS J142435.97+421030.4	2.213	16.28	16.01	15.01	2020 Jul 10	2020A	1800	$\cdots$	$\cdots$	$\cdots$
SDSS J142500.24+494729.2	2.260	16.52	15.80	15.22	2020 Mar 11	2020A	1800	$\cdots$	1	$\cdots$
SDSS J142502.62+274912.2	2.344	16.74	15.94	14.88	2020 Jun 29	2020A	1800	$\cdots$	$\cdots$	$\cdots$
SDSS J142543.32+540619.3	3.247	16.06	15.50	15.24	2020 Mar 11	2020A	1800	$\cdots$	$\cdots$	$\cdots$
SDSS J142903.03−014519.3	3.420	16.52	15.74	15.06	2019 May 14	2019A	1800	$\cdots$	$\cdots$	$\cdots$
SDSS J144624.29+173128.8	2.196	16.56	15.76	15.42	2018 Jun 26	2018A	1800	$\cdots$	$\cdots$	$\cdots$
SDSS J144706.29+350956.1	2.273	16.26	15.72	14.83	2019 Mar 21	2019A	1800	4	1	$\cdots$
SDSS J144706.81+212839.2	3.235	16.47	15.82	15.29	2020 Jun 30	2020A	1800	$\cdots$	$\cdots$	$\cdots$
SDSS J144948.62+123047.5	1.592	16.55	15.51	15.34	2019 Apr 23	2019A	1800	$\cdots$	$\cdots$	$\cdots$
SDSS J145541.11−023751.0	1.613	16.58	16.05	14.78	2020 Jul 08	2020A	1800	$\cdots$	$\cdots$	$\cdots$
SDSS J145608.33+111823.7	1.562	16.37	15.40	14.94	2019 Mar 22	2019A	1800	4	$\cdots$	$\cdots$
SDSS J150205.58−024038.5	2.215	16.49	15.84	15.14	2019 Apr 18	2019A	1800	$\cdots$	1	$\cdots$
SDSS J150226.60+180039.5	2.340	16.02	15.26	14.79	2020 Feb 23	2020A	1600	4	1	$\cdots$
SDSS J150743.71+220928.8	3.236	16.57	16.06	15.35	2020 Jun 04	2020A	1800	$\cdots$	$\cdots$	$\cdots$
SDSS J151123.30+495101.2	2.400	16.09	15.47	14.77	2019 Apr 24	2019A	1800	$\cdots$	1	$\cdots$
SDSS J151341.89+463002.8	1.579	16.60	15.62	15.57	2019 Apr 17	2019A	1800	$\cdots$	1	$\cdots$
SDSS J151507.82+612411.9	2.182	16.74	15.58	15.23	2020 Jun 14	2020A	1800	$\cdots$	$\cdots$	$\cdots$
SDSS J151727.68+133358.6	2.235	16.48	15.84	14.94	2019 Apr 23	2019A	1800	$\cdots$	$\cdots$	$\cdots$
SDSS J151733.09+435648.4	2.197	16.56	15.99	15.24	2020 Jun 04	2020A	1800	$\cdots$	$\cdots$	$\cdots$
SDSS J152336.27+071325.7	1.586	16.43	15.42	15.36	2019 Mar 22	2019A	1800	4	1	$\cdots$
SDSS J152929.55+230208.7	1.581	16.52	15.69	15.66	2019 Apr 16	2019A	1800	$\cdots$	$\cdots$	$\cdots$
SDSS J153248.95+173900.8	2.350	16.69	15.70	15.37	2019 Apr 23	2019A	1800	$\cdots$	1	$\cdots$
SDSS J153551.23+373029.0	2.197	16.64	15.94	14.85	2020 Jul 01	2020A	1800	4	$\cdots$	$\cdots$
SDSS J154231.96+390854.8	2.356	17.01	15.74	15.24	2020 Jul 01	2020A	1720	4	$\cdots$	$\cdots$
SDSS J154550.37+554346.2	2.158	16.15	15.49	14.99	2018 Jul 31	2018A	920	3	1	$\cdots$
SDSS J154907.47+565645.7	1.603	16.56	15.76	15.33	2020 Aug 01	2020A	1800	4	$\cdots$	$\cdots$
SDSS J155355.10+375844.1	2.369	16.89	15.96	15.19	2020 Jul 28	2020A	1800	$\cdots$	$\cdots$	$\cdots$
SDSS J155934.26+590031.6	1.601	16.54	15.52	15.12	2020 Jun 14	2020A	1720	4	$\cdots$	$\cdots$
SDSS J160029.86+331806.9	1.593	16.61	15.83	15.27	2018 Jun 26	2018A	1800	$\cdots$	$\cdots$	$\cdots$
SDSS J160137.90+172851.0	2.239	15.69	15.90	14.87	2020 Jun 04	2020A	1800	4	$\cdots$	$\cdots$
SDSS J160207.67+380743.0	1.593	15.29	14.51	14.39	2018 Jun 04	2018A	640	$\cdots$	1	$\cdots$
SDSS J160425.30+193929.1	3.313	16.55	16.05	15.15	2019 Jan 09	2018B	900	$\cdots$	$\cdots$	$\cdots$

Table 1 continued

Table 1 *(continued)*

Quasar	z_{SDSS}[a]	J	H	K	Obs. Date	Semester	Net Exp.	Comments	BAL	RL
		[mag]	[mag]	[mag]			[s]			
(1)	(2)	(3)	(4)	(5)	(6)	(7)	(8)	(9)	(10)	(11)
SDSS J160513.17+325829.9	2.276	16.49	15.97	15.42	2020 Jun 28	2020A	1800	⋯	⋯	⋯
SDSS J160552.97+292141.4	2.321	16.25	15.44	14.70	2019 Jan 10	2018B	920	⋯	1	⋯
SDSS J160637.57+173516.2	2.323	16.72	16.00	15.75	2020 Jul 11	2020A	1800	⋯	⋯	⋯
SDSS J160716.65+182649.4	2.323	16.48	15.83	14.97	2020 Jul 08	2020A	1800	4	⋯	⋯
SDSS J161435.70+372715.6	1.601	15.85	14.94	14.84	2020 Jun 30	2020A	1200	⋯	⋯	⋯
SDSS J161942.39+525613.4	2.345	15.55	14.83	13.95	2019 Apr 24	2019A	1800	⋯	⋯	1
SDSS J161942.58+325419.3	2.220	16.50	15.94	15.46	2020 Jun 29	2020A	1800	4	⋯	⋯
SDSS J162659.24+301535.0	1.578	16.45	15.81	15.43	2020 Jul 05	2020A	1800	⋯	⋯	1
SDSS J162701.94+313549.2	2.318	16.01	15.63	14.74	2018 Jun 26	2018A	1800	4	⋯	⋯
SDSS J163125.10+174810.0	2.180	16.15	15.38	14.44	2020 Jun 04	2020A	1600	⋯	1	⋯
SDSS J163433.42+265158.2	1.571	16.44	15.73	15.57	2020 Jul 05	2020A	1800	⋯	⋯	⋯
SDSS J164807.55+254407.1	2.191	15.71	15.16	14.35	2019 Apr 15	2019A	1800	⋯	⋯	⋯
SDSS J165321.03+271706.7	1.605	15.71	15.08	14.67	2020 Jun 15	2020A	1600	⋯	⋯	⋯
SDSS J165348.02+485019.0	2.249	16.18	15.44	15.01	2018 May 13	2018A	920	1,4	⋯	⋯
SDSS J174015.84+255457.1	2.220	16.61	16.01	15.46	2020 Jul 03	2020A	1800	4	⋯	⋯
SDSS J205900.36−064309.5	2.280	16.55	15.86	15.40	2018 Jun 29	2018B	1800	⋯	⋯	⋯
SDSS J210831.56−063022.5	2.345	16.43	15.78	15.08	2018 Jun 06	2018A	1800	⋯	⋯	⋯
SDSS J214611.80−085857.4	2.182	16.67	15.86	15.30	2018 Jun 29	2018B	1800	4	⋯	⋯
SDSS J214657.66−023946.3	2.283	16.44	16.09	15.32	2019 Oct 31	2019B	1800	4	⋯	⋯
SDSS J214901.21−073141.6	2.211	16.86	15.92	15.69	2018 Jul 19	2018A	1800	2	⋯	⋯
SDSS J220344.98+235729.3	2.187	17.54	16.08	15.52	2019 Sep 08	2019B	1800	⋯	1	⋯
SDSS J222621.45+251545.0	2.385	14.88	14.31	13.51	2017 Nov 05	2017B	600	⋯	⋯	⋯
SDSS J223934.45−004707.2	2.221	16.91	15.97	15.70	2018 Jul 28	2018A	1800	3	1	⋯
SDSS J225608.48+010557.8	2.268	16.78	15.86	15.23	2018 Jul 19	2018A	1800	⋯	1	⋯
SDSS J225627.12+092313.3	2.290	16.67	15.86	15.42	2018 Jul 01	2018B	1800	⋯	⋯	⋯
SDSS J230722.21+253803.8	1.594	16.40	15.53	15.46	2018 Jul 12	2018A	1800	⋯	⋯	⋯
SDSS J231450.12+182402.8	2.284	16.58	15.95	15.14	2018 Jul 01	2018B	1800	⋯	⋯	⋯
SDSS J231706.96+323802.8	2.378	16.97	16.07	15.73	2019 Oct 18	2019B	1800	4	⋯	⋯
SDSS J233344.66+290251.5	3.201	16.81	16.04	15.76	2019 Oct 31	2019B	1800	⋯	⋯	⋯
SDSS J234817.55+193345.8	2.154	16.69	15.96	15.33	2018 Jun 30	2018B	1800	⋯	⋯	⋯
SDSS J235212.85−012029.6	2.376	16.85	15.84	15.36	2017 Sep 09	2017B	1800	⋯	⋯	⋯

[a] Value based on best available measurement as stated by SDSS (Pâris et al. 2018, Table A1, column 9 "Z").

Note—Objects followed by an empty row aside from observation date, semester, and net exposure are additional observations made for that same object.
Comments:
(1) At least one exposure was taken under subpar observing conditions.
(2) All exposures were taken under supbar observing conditions.
(3) Supplemental data used from other observations to aid in reduction as described in Section 4.5.
(4) Observation failed to provide spectrum of the source due to bad weather, instrument artifacts, or other technical difficulties during the observation.

Table 2. Column Headings for Spectral Measurements

Column	Name	Bytes	Format	Units	Description
(1)	(2)	(3)	(4)	(5)	(6)
1	OBJ	(1-24)	A24	$\cdots$	SDSS object designation
2	ZSYS	(26-29)	F4.3	$\cdots$	Systemic redshifts
3	LC_MG II	(31-35)	F5.0	Å	Observed-frame wavelength of the emission line peak of Mg II based on peak fit value
4	LC_MG II_UPP	(37-39)	F3.0	Å	Upper uncertainty for the line peak of Mg II
5	LC_MG II_LOW	(41-43)	F3.0	Å	Lower uncertainty for the line peak of Mg II
6	FWHM_MG II	(45-48)	F4.0	km s^{-1}	FWHM of Mg II
7	FWHM_MG II_UPP	(50-52)	F3.0	km s^{-1}	Upper uncertainty of FWHM of Mg II
8	FWHM_MG II_LOW	(54-56)	F3.0	km s^{-1}	Lower uncertainty of FWHM of Mg II
9	EW_MG II	(58-59)	F2.0	Å	Rest-frame EW of Mg II
10	EW_MG II_UPP	(61-62)	F2.0	Å	Upper uncertainty of EW of Mg II
11	EW_MG II_LOW	(64-65)	F2.0	Å	Lower uncertainty of EW of Mg II
12	AS_MG II	(67-71)	E5.2	$\cdots$	Asymmetry of the double Gaussian fit profile of Mg II
13	KURT_MG II	(73-75)	F3.2	$\cdots$	Kurtosis of the double Gaussian fit profile of Mg II
14	LC_HB	(77-81)	F5.0	Å	Observed-frame wavelength of the emission line peak of Hβ based on peak fit value
15	LC_HB_UPP	(83-85)	F3.0	Å	Upper uncertainty for the line peak of Hβ
16	LC_HB_LOW	(87-89)	F3.0	Å	Lower uncertainty for the line peak of Hβ
17	FWHM_HB	(91-94)	F4.0	km s^{-1}	FWHM of Hβ
18	FWHM_HB_UPP	(96-98)	F3.0	km s^{-1}	Upper uncertainty of FWHM of Hβ
19	FWHM_HB_LOW	(100-102)	F3.0	km s^{-1}	Lower uncertainty of FWHM of Hβ
20	EW_HB	(104-105)	F2.0	Å	Rest-frame EW of Hβ
21	EW_HB_UPP	(107-108)	F2.0	Å	Upper uncertainty of EW of Hβ
22	EW_HB_LOW	(110-111)	F2.0	Å	Lower uncertainty of EW of Hβ
23	AS_HB	(113-17)	E5.2	$\cdots$	Asymmetry of the double Gaussian fit profile of Hβ
24	KURT_HB	(119-121)	F3.2	$\cdots$	Kurtosis of the double Gaussian fit profile of Hβ
25	LC_O III	(123-127)	F5.0	Å	Observed-frame wavelength of the emission line peak of [O III] λ5007 based on peak fit value
26	LC_O III_UPP	(129-131)	F3.0	Å	Upper uncertainty for the line peak of [O III] λ5007
27	LC_O III_LOW	(133-135)	F3.0	Å	Lower uncertainty for the line peak of [O III] λ5007
28	FWHM_O III	(137-140)	F4.0	km s^{-1}	FWHM of [O III] λ5007
29	FWHM_O III_UPP	(142-144)	F3.0	km s^{-1}	Upper uncertainty of FWHM of [O III] λ5007
30	FWHM_O III_LOW	(146-148)	F3.0	km s^{-1}	Lower uncertainty of FWHM of [O III] λ5007
31	EW_O III	(150-151)	F2.0	Å	Rest-frame EW of [O III] λ5007
32	EW_O III_UPP	(153-154)	F2.0	Å	Upper uncertainty of EW of [O III] λ5007
33	EW_O III_LOW	(156-157)	F2.0	Å	Lower uncertainty of EW of [O III] λ5007
34	AS_O III	(159-163)	E5.2	$\cdots$	Asymmetry of the double Gaussian fit profile of [O III] λ5007
35	KURT_O III	(165-167)	F3.2	$\cdots$	Kurtosis of the double Gaussian fit profile of [O III] λ5007
36	LC_HA	(169-173)	F5.0	Å	Observed-frame wavelength of the emission line peak of Hα based on peak fit value
37	LC_HA_UPP	(175-177)	F3.0	Å	Upper uncertainty for the line peak of Hα
38	LC_HA_LOW	(179-181)	F3.0	Å	Lower uncertainty for the line peak of Hα
39	FWHM_HA	(183-186)	F4.0	km s^{-1}	FWHM of Hα
40	FWHM_HA_UPP	(188-190)	F3.0	km s^{-1}	Upper uncertainty of FWHM of Hα
41	FWHM_HA_LOW	(192-194)	F3.0	km s^{-1}	Lower uncertainty of FWHM of Hα
42	EW_HA	(196-197)	F2.0	Å	Rest-frame EW of Hα
43	EW_HA_UPP	(199-200)	F2.0	Å	Upper uncertainty of EW of Hα
44	EW_HA_LOW	(202-203)	F2.0	Å	Lower uncertainty of EW of Hα
45	AS_HA	(205-209)	E5.2	$\cdots$	Asymmetry of the double Gaussian fit profile of Hα
46	KURT_HA	(211-213)	F3.2	$\cdots$	Kurtosis of the double Gaussian fit profile of Hα
47	FWHM_FE II	(215-218)	F4.0	km s^{-1}	FWHM of the kernel Gaussian used to broaden the Fe II template
48	EW_FE II[a]	(220-221)	F2.0	Å	Rest-frame EW of Fe II in the optical as defined by Boroson, & Green (1992)
49	LOGFλ5100	(223-227)	E5.2	erg s^{-1}cm^{-2}Å^{-1}	Flux density at rest-frame 5100 Å
50	LOGL5100	(229-232)	F4.2	erg s^{-1}	Monochromatic luminosity at rest-frame 5100 Å

NOTE—Data formatting used for the catalog. Asymmetry is defined here as the skewness of the Gaussian fits, i.e., a measure of the asymmetry of the distribution about its mean, $s = E(x - \mu)^3/\sigma^3$, where μ is the mean of x, σ is the standard deviation of x, and $E(t)$ is the expectation value. Kurtosis is the quantification of the "tails" of the Gaussian fits defined as $k = E(x - \mu)^4/\sigma^4$, where symbols are the same as for asymmetry.

[a] A value of 2 Å denotes an upper limit on this parameter.

Table 3. Column Headings for Supplemental Emission-Line Measurements

Column	Name	Bytes	Format	Units	Description
(1)	(2)	(3)	(4)	(5)	(6)
1	OBJ	(1-24)	A24	$\cdots$	SDSS object designation
2	LC_HD	(26-30)	F5.0	Å	Observed-frame wavelength of the emission line peak of Hδ based on peak fit value
3	LC_HD_UPP	(32-35)	F4.0	Å	Upper uncertainty for the line peak of Hδ
4	LC_HD_LOW	(37-40)	F4.0	Å	Lower uncertainty for the line peak of Hδ
5	FWHM_HD	(42-45)	F4.0	km s^{-1}	FWHM of Hδ
6	FWHM_HD_UPP	(47-49)	F3.0	km s^{-1}	Upper uncertainty of FWHM of Hδ
7	FWHM_HD_LOW	(51-53)	F3.0	km s^{-1}	Lower uncertainty of FWHM of Hδ
8	EW_HD	(55-56)	F2.0	Å	Rest-frame EW of Hδ
9	EW_HD_UPP	(58-59)	F2.0	Å	Upper uncertainty of EW of Hδ
10	EW_HD_LOW	(61-62)	F2.0	Å	Lower uncertainty of EW of Hδ
11	AS_HD	(64-68)	E5.2	$\cdots$	Asymmetry of the double Gaussian fit profile of Hδ
12	KURT_HD	(70-72)	F3.2	$\cdots$	Kurtosis of the double Gaussian fit profile of Hδ
13	LC_HG	(74-78)	F5.0	Å	Observed-frame wavelength of the emission line peak of Hγ based on peak fit value
14	LC_HG_UPP	(80-83)	F4.0	Å	Upper uncertainty for the line peak of Hγ
15	LC_HG_LOW	(85-88)	F4.0	Å	Lower uncertainty for the line peak of Hγ
16	FWHM_HG	(90-93)	F4.0	km s^{-1}	FWHM of Hγ
17	FWHM_HG_UPP	(95-97)	F3.0	km s^{-1}	Upper uncertainty of FWHM of Hγ
18	FWHM_HG_LOW	(99-101)	F3.0	km s^{-1}	Lower uncertainty of FWHM of Hγ
19	EW_HG	(103-104)	F2.0	Å	Rest-frame EW of Hγ
20	EW_HG_UPP	(106-107)	F2.0	Å	Upper uncertainty of EW of Hγ
21	EW_HG_LOW	(109-110)	F2.0	Å	Lower uncertainty of EW of Hγ
22	AS_HG	(112-116)	E5.2	$\cdots$	Asymmetry of the double Gaussian fit profile of Hγ
23	KURT_HG	(118-120)	F3.2	$\cdots$	Kurtosis of the double Gaussian fit profile of Hγ
24	LC_O II[a]	(122-126)	F5.0	Å	Observed-frame wavelength of the emission line peak of [O II] based on peak fit value
25	LC_O II_UPP	(128-131)	F4.0	Å	Upper uncertainty for the line peak of [O II]
26	LC_O II_LOW	(133-136)	F4.0	Å	Lower uncertainty for the line peak of [O II]
27	FWHM_O II	(138-141)	F4.0	km s^{-1}	FWHM of [O II]
28	FWHM_O II_UPP	(143-145)	F3.0	km s^{-1}	Upper uncertainty of FWHM of [O II]
29	FWHM_O II_LOW	(147-149)	F3.0	km s^{-1}	Lower uncertainty of FWHM of [O II]
30	EW_O II	(151-152)	F2.0	Å	Rest-frame EW of [O II]
31	EW_O II_UPP	(154-155)	F2.0	Å	Upper uncertainty of EW of [O II]
32	EW_O II_LOW	(157-158)	F2.0	Å	Lower uncertainty of EW of [O II]
33	AS_O II	(160-164)	E5.2	$\cdots$	Asymmetry of the double Gaussian fit profile of [O II]
34	KURT_O II	(166-168)	F3.2	$\cdots$	Kurtosis of the double Gaussian fit profile of [O II]
35	LC_NE III[b]	(170-174)	F5.0	Å	Observed-frame wavelength of the emission line peak of [Ne III] based on peak fit value
36	LC_NE III_UPP	(176-179)	F4.0	Å	Upper uncertainty for the line peak of [Ne III]
37	LC_NE III_LOW	(181-184)	F4.0	Å	Lower uncertainty for the line peak of [Ne III]
38	FWHM_NE III	(186-189)	F4.0	km s^{-1}	FWHM of [Ne III]
39	FWHM_NE III_UPP	(191-193)	F3.0	km s^{-1}	Upper uncertainty of FWHM of [Ne III]
40	FWHM_NE III_LOW	(195-197)	F3.0	km s^{-1}	Lower uncertainty of FWHM of [Ne III]
41	EW_NE III	(199-200)	F2.0	Å	Rest-frame EW of [Ne III]
42	EW_NE III_UPP	(202-203)	F2.0	Å	Upper uncertainty of EW of [Ne III]
43	EW_NE III_LOW	(205-206)	F2.0	Å	Lower uncertainty of EW of [Ne III]
44	AS_NE III	(208-212)	E5.2	$\cdots$	Asymmetry of the double Gaussian fit profile of [Ne III]
45	KURT_NE III	(214-216)	F3.2	$\cdots$	Kurtosis of the double Gaussian fit profile of [Ne III]

NOTE—Data formatting used for the supplemental measurements in the supplemental features catalog.

[a] [O II] λ 3727

[b] [Ne III] λ 3870